Strain gradient crystal plasticity with evolving length scale: Application to voided irradiated materials

J.M. Scherer, Jacques Besson, Samuel Forest, Jérémy Hure, B. Tanguy

Strain gradient crystal plasticity with evolving length scale: Application to voided irradiated materials[1]

J.M. Scherer[a,b], J. Besson[b], S. Forest[b], J. Hure[a], B. Tanguy[a]

[a] *DEN-Service d'Études des Matériaux Irradiés, CEA, Université Paris-Saclay, F-91191, Gif-sur-Yvette, France*
[b] *MINES ParisTech, PSL Research University, MAT – Centre des matériaux, CNRS UMR 7633, BP 87 91003 Evry, France*

Abstract

A micromorphic crystal plasticity model is used to simulate slip band localization in single crystals under simple shear at finite deformations. Closed form analytical solutions are derived for single slip in the case of positive, zero and negative strain hardening. Linear negative strain hardening, i.e. linear softening, leads to a constant localization slip band width, while non linear softening and saturating behaviour results in an increasing band width. An enhanced model is therefore proposed in order to maintain a bounded localization slip band width when considering an exponential softening behaviour. Analytical solutions are used to validate finite element computation of the same boundary value problems. The enhanced micromorphic crystal plasticity model is then applied to predict the interaction between localized slip bands and voids encountered in porous irradiated materials. For that purpose, periodic porous unit cells are loaded in simple shear with a strain gradient crystal plasticity matrix material. The finite element simulation results show that, for a given void volume fraction, the larger the voids, the wider the localization band. However, for a given void size, the larger the void volume fraction, the narrower the localization band. In addition a satisfactory qualitative agreement of the rotation and elongation of the voids with the experimental observations made in irradiated materials is observed, where small voids are shown to remain ellipsoidal for larger shear strains. Large voids deform into peanut-like shapes.

Keywords: Strain Gradient Crystal Plasticity, Micromorphic approach, Slip band localization, Ductile fracture, Void shearing, Irradiated materials

1. Introduction

Strain localization is commonly encountered in experiments involving a wide range of materials at scales spanning over multiple orders of magnitude and are referred to as necking, shear bands, Lüders bands, Portevin-Le Chatelier effect. The pioneering works of Considère (1885); Hadamard (1903); Thomas (1961); Hill (1962); Mandel (1966); Rice (1976) set the general framework for predicting strain localization as a result of a mechanical instability involving either geometric or material imperfections. In metals, a material-based instability may for example originate from a porosity growth

[1] This article was presented at the IUTAM Symposium on Size-Effects in Microstructure and Damage Evolution at Technical University of Denmark, 2018

induced softening behaviour leading to shear-banding, while necking in a tensile test is an example of a geometry-based instability (Hart, 1967; Audoly and Hutchinson, 2018). In single crystals slip bands and kink bands described in (Gilman, 1954; Jaoul, (1965, 2008); Neuhäuser, 1983b) are common occurrences of material induced strain localization phenomena. Characteristic length scales arise naturally in strain localization phenomena observed in experiments, but conventional material models are however size-independent and therefore cannot provide satisfying predictions for strain localization. In addition when aiming at modelling softening mechanisms, numerical simulations using conventional theories display spurious mesh dependent dissipated energy due to the loss of ellipticity of the underlying partial differential equations (see e.g. Bažant et al. (1984); Lorentz and Benallal (2005); Germain et al. (2007)). As a remedy, regularization methods such as Cosserat, integral and gradient models (see (Forest, 2005) and references quoted therein) have been developed extensively in the past few decades also motivated by size effects observed in experiments. In particular, observations suggest that some size effects in metals are related to Geometrically Necessary Dislocations (GND) (Stelmashenko et al., 1993; Fleck and Hutchinson, 1997). Hence strain gradient plasticity (SGP) theories have been extended to frameworks suited to (sub-)crystalline scales, as for instance continuum crystal plasticity ((Fleck and Hutchinson, 1997; Forest et al., 2000; Bardella, 2006; Cordero et al., 2010; Niordson and Kysar, 2014) and references quoted therein).

For metallic single crystals strain localization induced by material softening generally results in the formation of slip bands. These thin bands are parallel to the primary slip plane and their thickness is directly related to the defect density and softening mechanism involved. In contrast, kink bands are localization zones of finite thickness that are perpendicular to the slip direction. Kink bands are known to occur when strain incompatibility arises and if not enough slip systems are available. Asaro and Rice (1977) have performed a bifurcation analysis of plastic slip localization for crystals undergoing single slip. Their theoretical analysis shows that slip and kink bands are equally probable single slip localization modes in that conditions. Asaro and Rice's bifurcation analysis is based on standard crystal plasticity. More advanced crystal plasticity models incorporate the dislocation density tensor as a hardening variable in addition to scalar dislocation densities (statistically stored dislocations) (Gurtin, 2002; Wulfinghoff et al., 2015). Dislocation pile-ups are known to induce a back-stress and associated kinematic hardening (Steinmann and Stein, 1996; Forest, 2008; Cordero et al., 2010). As a result localization in kink bands can be superseded by slip bands that do not induce any lattice curvature as proved by the bifurcation analysis in (Forest, 1998). Strain gradient plasticity introduces length scales in the continuum models and can therefore provide physically-relevant regularization properties. It appears that strain gradient plasticity regularizes kink bands, meaning that simulated kink bands have a finite thickness (Forest et al., 2001). In contrast the finite element simulation of slip bands is mesh–dependent (they are one element (in fact one Gauss point) thick) because they can develop in the absence of accumulation of GND. The recent simplified strain gradient plasticity model developed by Ling et al. (2018), following the approach from Wulfinghoff and Böhlke (2012); Wulfinghoff et al. (2013), displays the unique feature of regularizing both slip and kink bands. This is

because it involves the full gradient of a cumulated slip variable instead of the dislocation density tensor or individual GND densities. This model is acknowledged to be too crude to control independently the intensity of slip and kink bands. The regularization effect on slip bands is of phenomenological nature, it has no precise physical background in contrast to kink bands which are controlled by the formation of polarized dislocation walls represented by GND densities. It is a necessary feature for a model to be used in mesh–objective finite element simulations of slip banding in crystals.

Although it is of particular importance when investigating flow localization, only a few works mention the evolution of the length scale during straining and how it is linked to the hardening/softening behaviour. In an early work Zbib and Aifantis (1988) highlighted the slip band narrowing arising when considering a parabolic hardening/softening behaviour in a strain gradient framework. In the different but closely related context of non-local damage models, Geers et al. (1998); Simone et al. (2004) evidenced spurious spreading of damage over continuously wider regions. Recently Poh and Sun (2017) and Vandoren and Simone (2018) proposed to use a damage-dependent length scale respectively in micromorphic and integral non-local damage models to address this unwanted phenomenon. Dislocations motion mechanisms motivated Forest and Sedláček (2003) to propose evolving length scales depending on the dislocation density. Dahlberg and Boasen (2019) provided a strain gradient framework incorporating an evolution law for the constitutive length scale parameter which is also physically based and directly related to the dislocation density. Evolving length scales are also present in the newly developed SGP model by Petryk and Stupkiewicz (2016). Also, to the authors' knowledge, the case of saturating softening behaviour has received little attention in the literature. This is particularly important when aiming at simulating ductile failure at large local strains of materials exhibiting softening. We will show in the present work that the saturated regime in most existing SGP models leads to unwanted broadening of the localization zone. This feature will be analyzed and a remedy will be proposed.

One example of intense flow localization is the mechanism of dislocation channel deformation (DCD). It consists in a highly heterogeneous deformation mode at the grain scale. Abundant observations of this deformation mode have been made in quenched (Bapna et al., 1968; Mori and Meshii, 1969; Wechsler, 1973), predeformed (Luft et al., 1975) and irradiated (Tucker et al., 1969; Smidt Jr, 1970; Wechsler, 1973; Fish et al., 1973; Farrell et al., 2003; Jiao and Was, 2010; Gussev et al., 2015) metals. Such channels initiate when the first moving dislocations are clearing a path of isolated sessile obstacles, for example Frank dislocation loops, leading to a reduced defect density inside channels. They are also called clear bands due to their contrast in electron microscopy (Lee et al., 2001). The induced softening along that path is the precursor to flow localization. It has been shown experimentally in (Farrell et al., 2003) and numerically in (Barton et al., 2013; Arsenlis et al., 2012; Cui et al., 2018) that deformation localization in irradiated steels is simultaneously accompanied by a loss of dislocation interactions and activation of fewer slip systems. The thickness of dislocation channels is typically measured in a 10 nm to 100 nm range in irradiated materials (Farrell et al., 2003). Dislocation channels are known to have a strong influence on macroscopic mechanical properties of nuclear

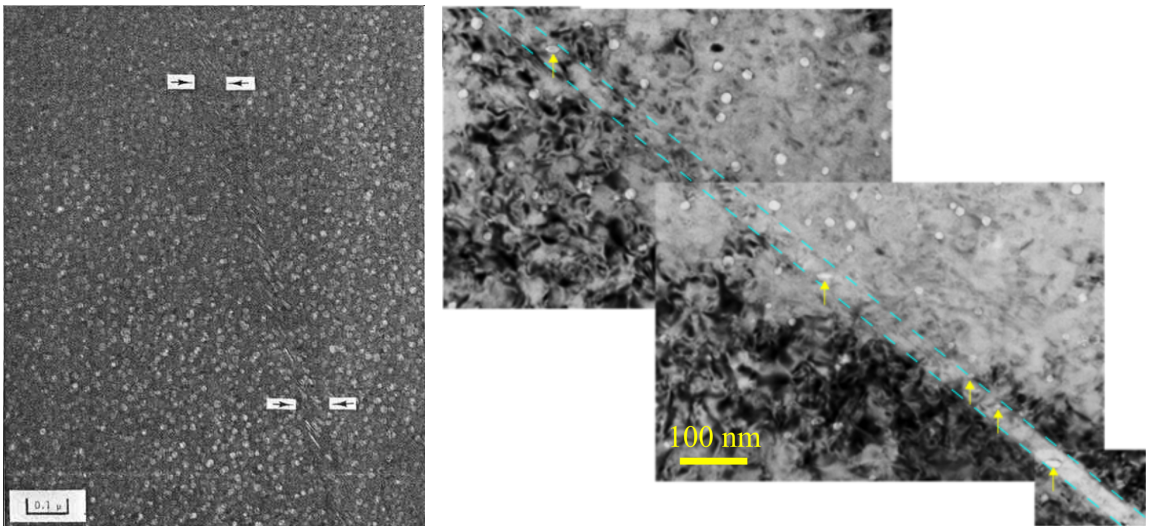

(a) (b)

Fig. 1: (a) Dislocation channeling observed by TEM in a highly irradiated (7.5×10^{22} n/cm^2, $E > 0.1$ MeV) deformed tension specimen tested (stainless steel 316) at 370 °C (reproduced from (Fish et al., 1973)) displaying peanut-like void shapes (b) Deformed neutron irradiated stainless steel 316 at 340 °C displaying sheared and elongated irradiation voids (pointed out with yellow arrows) inside a dislocation channel (bounded by cyan dashed lines) (reproduced from (Renault-Laborne et al., 2018))

materials. Dislocation channels may indeed interact with grain boundaries and favor the mechanism of Irradiation Assisted Stress Corrosion Cracking (IASSC) (McMurtrey et al., 2011). Moreover the Transmission Electron Microscope (TEM) observations of deformed radiation-damaged stainless steels in figures 1a and 1b suggest that dislocation channels may also interact with other irradiation induced defects such as nanometric voids or bubbles. Elongated voids inside channels indicate possible large local strains.

In this study a reduced finite strain micromorphic single crystal plasticity model is used to describe slip band localization in single crystals. The novelty of the approach lies first in the analytical derivation of closed form solutions obtained from a micromorphic crystal plasticity theory in case of single slip associated to linear hardening and softening behaviours. It is demonstrated that this kind of model predicts an increasing and unbounded localization slip band width when a saturation of softening is reached. Second, an enhanced micromorphic crystal plasticity model, involving an evolving length scale, is then proposed that predicts a bounded localization slip band width for realistic saturating softening behaviours. Finally, the enhanced model is applied to study the interaction between localization slip bands and voids that may exist or nucleate in irradiated materials. For that purpose a 2D plane strain periodic porous unit cell containing one void is loaded in simple shear with the shearing direction parallel to the single slip direction. A simple exponential softening behaviour is used in order to model softening due to irradiation defects clearing by the DCD mechanism. The relative influence on localization of the intrinsic length scale of the micromorphic crystal plasticity model and of the void size and effective void volume fraction inside the localization slip band are

assessed.

The paper is outlined as follows. In section 2 the main features of the micromorphic crystal plasticity model are presented and analytical reference solutions for single crystals under simple shear are derived, assuming single slip and linear hardening behaviour. An analytical solution for linear softening is established showing constant slip band width. An enhanced model is then proposed in order to keep a bounded localization slip band width for non-linear softening behaviour in section 3. In section 2 and 3, numerical solutions are compared to the analytical solutions. Finite element predictions of void / localization band interactions are presented and discussed in section 4 for 2D plane strain periodic porous unit cells. Concluding remarks follow in section 5.

2. Simple shear in the cases of linear hardening and perfect plasticity

The model used in the next sections is taken from (Ling et al., 2018) and synoptically recalled hereafter. It is based on initial formulations by Wulfinghoff and Böhlke (2012); Erdle and Böhlke (2017) and finite deformation extensions from (Forest, 2016). Underline $\underline{A}$ and under-wave bold $\underset{\sim}{\boldsymbol{A}}$ symbols refer to vectors and second-order tensors, respectively. Dyadic product, outer product, double contraction and tensorial product are respectively written $\underline{\boldsymbol{A}}.\underline{\boldsymbol{B}}$, $\underline{\boldsymbol{A}} \wedge \underline{\boldsymbol{B}}$, $\underset{\sim}{\boldsymbol{A}} : \underset{\sim}{\boldsymbol{B}}$ and $\underline{\boldsymbol{A}} \otimes \underline{\boldsymbol{B}}$. Transposition, inversion, inversion followed by transposition and time derivation are respectively written $\underset{\sim}{\boldsymbol{A}}^T$, $\underset{\sim}{\boldsymbol{A}}^{-1}$, $\underset{\sim}{\boldsymbol{A}}^{-T}$, $\dot{\underset{\sim}{\boldsymbol{A}}}$.

2.1. A reduced micromorphic single crystal plasticity model at finite deformations

Let us consider a crystalline continuum for which each material point can uniquely be defined by a position vector $\underline{\boldsymbol{X}}$ in the reference configuration Ω_0 and a position vector $\underline{\boldsymbol{x}}$ in the current configuration Ω. Following the micromorphic approach of (Germain, 1973; Forest, 2016), at time t, the degrees of freedom (DOF) of the material point are described by the field of displacement vector $\underline{\boldsymbol{u}}\,(\underline{\boldsymbol{X}}\,,t)$ and an additional microslip scalar field $\gamma_\chi(\underline{\boldsymbol{X}}\,,t)$. This additional field of degrees of freedom γ_χ, which comes in addition to usual constitutive internal variables, is introduced to refine the kinematical description at a given material point $\underline{\boldsymbol{X}}$:

$$\text{DOF} = \{\underline{\boldsymbol{u}}\,, \gamma_\chi\}. \tag{1}$$

In the present work, the micromorphic variable γ_χ is akin to a cumulative plastic slip variable within the micromorphic approach (Forest, 2016). It will serve as an auxiliary variable for a convenient numerical implementation of strain gradient plasticity.

The Lagrangian gradients of the degrees of freedom are:

$$\underset{\sim}{\boldsymbol{H}}(\underline{\boldsymbol{x}}\,,t) = \frac{\partial \underline{\boldsymbol{u}}}{\partial \underline{\boldsymbol{X}}} = \text{Grad}\,\underline{\boldsymbol{u}}\,, \tag{2}$$

$$\underline{\boldsymbol{K}}\,(\underline{\boldsymbol{x}}\,,t) = \frac{\partial \gamma_\chi}{\partial \underline{\boldsymbol{X}}} = \text{Grad}\,\gamma_\chi, \tag{3}$$

where the displacement gradient $\underset{\sim}{\boldsymbol{H}}$ is directly related to the deformation gradient $\underset{\sim}{\boldsymbol{F}}$ by $\underset{\sim}{\boldsymbol{F}} = \underset{\sim}{\mathbf{1}} + \underset{\sim}{\boldsymbol{H}}$, and $\underline{\boldsymbol{K}}$ is referred to as the microslip gradient vector. We introduce the following stresses:

$$\underset{\sim}{\boldsymbol{S}} = \frac{\rho_0}{\rho} \underset{\sim}{\boldsymbol{\sigma}} . \underset{\sim}{\boldsymbol{F}}^{-T}, \tag{4}$$

$$\underline{\boldsymbol{M}} = \frac{\rho_0}{\rho} \underset{\sim}{\boldsymbol{F}}^{-1} . \underline{\boldsymbol{m}}, \tag{5}$$

$$S = \frac{\rho_0}{\rho} s. \tag{6}$$

where $\underset{\sim}{\boldsymbol{S}}$ is the Boussinesq (or first Piola-Kirchhoff) stress tensor which generates mechanical power with $\dot{\underset{\sim}{\boldsymbol{F}}}$ and $\underset{\sim}{\boldsymbol{\sigma}}$ the Cauchy stress tensor which generates power with $\dot{\underset{\sim}{\boldsymbol{F}}} . \underset{\sim}{\boldsymbol{F}}^{-1}$. The vectors $\underline{\boldsymbol{M}}$ and $\underline{\boldsymbol{m}}$ are generalized stresses with respect to the reference and current configuration, respectively. They are respectively conjugate to $\dot{\underline{\boldsymbol{K}}}$ and $\dot{\underline{\boldsymbol{K}}} . \underset{\sim}{\boldsymbol{F}}^{-1}$ in the power of internal forces, see (Ling et al., 2018). Similarly, S and s are the generalized stresses in the reference and current configurations which generate power with $\dot{\gamma}_\chi$. The balance laws for momentum and generalized momentum take the form

$$\mathrm{Div}\, \underset{\sim}{\boldsymbol{S}} = \underline{\mathbf{0}}, \quad \forall \underline{\boldsymbol{X}} \in \Omega_0, \tag{7}$$

$$\mathrm{Div}\, \underline{\boldsymbol{M}} - S = 0, \quad \forall \underline{\boldsymbol{X}} \in \Omega_0, \tag{8}$$

where Ω_0 is the reference configuration of the body. The associated boundary conditions read

$$\underline{\boldsymbol{T}} = \underset{\sim}{\boldsymbol{S}} . \underline{\boldsymbol{n}}_0, \quad \forall \underline{\boldsymbol{X}} \in \partial\Omega_0, \tag{9}$$

$$M = \underline{\boldsymbol{M}} . \underline{\boldsymbol{n}}_0, \quad \forall \underline{\boldsymbol{X}} \in \partial\Omega_0, \tag{10}$$

where $\underline{\boldsymbol{T}}$ is the surface traction vector which generates power over $\dot{\underset{\sim}{\boldsymbol{F}}}$. M is the generalized surface traction which generates power over $\dot{\underline{\boldsymbol{K}}}$. Vector $\underline{\boldsymbol{n}}_0$ is the normal to the surface element of the boundary $\partial\Omega_0$ of the body. The multiplicative decomposition of the deformation gradient $\underset{\sim}{\boldsymbol{F}}$ is adopted

$$\underset{\sim}{\boldsymbol{F}} = \underset{\sim}{\boldsymbol{E}} . \underset{\sim}{\boldsymbol{P}}, \tag{11}$$

where $\underset{\sim}{\boldsymbol{E}}$ denotes its elastic part and $\underset{\sim}{\boldsymbol{P}}$ its plastic part. The local intermediate configuration $C_\sharp$ consists in the transport of the local reference configuration by the tensor $\underset{\sim}{\boldsymbol{P}}$. The local current configuration C consists in the transport of the reference configuration C_0 by $\underset{\sim}{\boldsymbol{F}}$, or equivalently the transport of $C_\sharp$ by $\underset{\sim}{\boldsymbol{E}}$. γ^s is the plastic slip on a system s defined by its Schmid tensor $\underset{\sim}{\boldsymbol{N}}^s = \underline{\boldsymbol{\ell}}^s \otimes \underline{\boldsymbol{n}}^s$ where $\underline{\boldsymbol{n}}^s$ is the normal to the slip plane and $\underline{\boldsymbol{\ell}}^s$ the slip direction. $\underset{\sim}{\boldsymbol{P}}$ is related to the plastic slips by

$$\dot{\underset{\sim}{\boldsymbol{P}}} . \underset{\sim}{\boldsymbol{P}}^{-1} = \sum_{s=1}^{N} \dot{\gamma}^s \underset{\sim}{\boldsymbol{N}}^s, \tag{12}$$

where N is the total number of slip systems. The elastic Green-Lagrange strain measure $\underset{\sim}{\boldsymbol{E}}^e_{GL}$ is introduced as

$$\underset{\sim}{\boldsymbol{E}}^e_{GL} = \frac{1}{2} \left(\underset{\sim}{\boldsymbol{E}}^T . \underset{\sim}{\boldsymbol{E}} - \underset{\sim}{\mathbf{1}} \right). \tag{13}$$

A plastic cumulated slip measure γ_{cum} is now defined as

$$\gamma_{cum} = \int_0^t \sum_{s=1}^{N} |\dot{\gamma}^s| \, \mathrm{d}t. \tag{14}$$

The relative plastic slip e quantifies the difference between cumulated plastic slip and microslip with

$$e(\underline{\boldsymbol{X}}, t) = \gamma_{cum} - \gamma_{\chi}. \tag{15}$$

γ_{χ} is the micromorhpic counterpart of γ_{cum}, they have identical physical interpretation.
A free energy density function ψ is chosen in the form:

$$\rho\psi(\underset{\sim}{\boldsymbol{E}}^e_{GL}, e, \underset{\sim}{\boldsymbol{K}}, \gamma_{cum}) = \frac{1}{2}\frac{\rho}{\rho_\sharp}\underset{\sim}{\boldsymbol{E}}^e_{GL} : \underset{\approx}{\boldsymbol{C}} : \underset{\sim}{\boldsymbol{E}}^e_{GL} + \frac{1}{2}\frac{\rho}{\rho_0}H_\chi e^2 + \frac{1}{2}\frac{\rho}{\rho_0}A\underline{\boldsymbol{K}}^T.\underline{\boldsymbol{K}} + \rho\psi_h(\gamma_{cum}), \tag{16}$$

$\underset{\approx}{\boldsymbol{C}}$ is the fourth rank tensor of elastic moduli, H_χ a penalty modulus, A a higher order modulus and ρ_0, $\rho_\sharp$ and ρ are volumetric mass densities in the reference, intermediate and final local configuration respectively. The function $\psi_h(\gamma_{cum})$ is a hardening potential which will take various forms in the following sections. For simplicity a quadratic and isotropic form was assumed for the gradient $\underline{\boldsymbol{K}}$ contribution in the free energy potential, leading to a single higher order modulus A. If the penalty modulus H_χ is large enough, the variable γ_χ is almost equal to γ_{cum}. In that case, the gradient $\underline{\boldsymbol{K}}$ of γ_χ does not significantly differ from the gradient of the cumulated slip variable γ_{cum}. In the following sections the following approximation will be used:

$$\gamma_\chi \simeq \gamma_{cum}, \quad \frac{\partial\gamma_\chi}{\partial\underline{\boldsymbol{X}}} \simeq \frac{\partial\gamma_{cum}}{\partial\underline{\boldsymbol{X}}}, \quad \frac{\partial^2\gamma_\chi}{\partial\underline{\boldsymbol{X}}^2} \simeq \frac{\partial^2\gamma_{cum}}{\partial\underline{\boldsymbol{X}}^2}. \tag{17}$$

When the penalty modulus H_χ takes a high enough value, γ_χ is almost equal to γ_{cum}. The micromorphic model then reduces to a SGP model (Forest, 2009). The following state laws are postulated, identically fulfilling the second law of thermodynamics:

$$\underset{\sim}{\boldsymbol{\Pi}}^e = \underset{\approx}{\boldsymbol{C}} : \underset{\sim}{\boldsymbol{E}}^e_{GL}, \tag{18}$$

$$S = -H_\chi e, \tag{19}$$

$$\underline{\boldsymbol{M}} = A\underline{\boldsymbol{K}}, \tag{20}$$

where the Piola (or second Piola-Kirchhoff) stress tensor $\underset{\sim}{\boldsymbol{\Pi}}^e$ is defined with respect to the intermediate configuration $C_\sharp$ by $\underset{\sim}{\boldsymbol{\Pi}}^e = \frac{\rho_\sharp}{\rho}\underset{\sim}{\boldsymbol{E}}^{-1}.\underset{\sim}{\boldsymbol{\sigma}}.\underset{\sim}{\boldsymbol{E}}^{-T} = \frac{\rho_\sharp}{\rho_0}\underset{\sim}{\boldsymbol{E}}^{-1}.\underset{\sim}{\boldsymbol{S}}.\underset{\sim}{\boldsymbol{P}}^T$. The Mandel stress $\underset{\sim}{\boldsymbol{\Pi}}^M$ is introduced with respect to the intermediate configuration by $\underset{\sim}{\boldsymbol{\Pi}}^M = \underset{\sim}{\boldsymbol{E}}^T.\underset{\sim}{\boldsymbol{E}}.\underset{\sim}{\boldsymbol{\Pi}}^e$, in order to compute the resolved shear stress τ^s by $\tau^s = \underset{\sim}{\boldsymbol{\Pi}}^M : \underset{\sim}{\boldsymbol{N}}^s$. In contrast to strict strain gradient plasticity, the higher order micromorphic stresses are uniquely defined in the elastic part of the structure. Whereas the slip variable γ vanishes in the elastic part, the microslip γ_χ can be different from zero. This occurs close to the boundary with the plastically active domain.

According to the second law of thermodynamics, the residual dissipation inequality is obtained as

$$\sum_{s=1}^{N}\left(|\tau^s| + \frac{\rho_\sharp}{\rho}s - \rho_\sharp\frac{\mathrm{d}\psi_h}{\mathrm{d}\gamma_{cum}}\right)|\dot{\gamma}^s| \geqslant 0. \tag{21}$$

Hence the yield function f^s for each slip system s is introduced with

$$f^s = |\tau^s| + \frac{\rho_\sharp}{\rho}s - \rho_\sharp\frac{\mathrm{d}\psi_h}{\mathrm{d}\gamma_{cum}} - \tau_0 = |\tau^s| - \left(\tau_0 - \frac{\rho_\sharp}{\rho}s + \rho_\sharp\frac{\mathrm{d}\psi_h}{\mathrm{d}\gamma_{cum}}\right), \tag{22}$$

where τ_0 is the initial critical resolved shear stress, which is assumed for brevity to be the same for all slip systems. For conciseness hardening is here assumed to be a function of γ_{cum} only. Noticing that $\rho_\sharp = \rho_0$ due to plastic incompressibility, from (6) one has $\frac{\rho_\sharp}{\rho} s = S$. Accordingly, a rate-dependent law is chosen for the plastic slip rates

$$\dot{\gamma}^s = \text{sign}\left(\tau^s\right) \dot{\gamma}_0 \left\langle \frac{|\tau^s| - \left(\tau_0 - S + \rho_\sharp \frac{\mathrm{d}\psi_h}{\mathrm{d}\gamma_{cum}}\right)}{\tau_0} \right\rangle^n . \tag{23}$$

where $\dot{\gamma}_0$ and n are viscosity parameters.

2.2. Analytical reference solutions for linear hardening and perfect plasticity

As a simple reference analysis of this model we propose to study the problem of a periodic unit cell loaded in simple shear and undergoing single slip for linear hardening and perfect plasticity behaviours. Predictions of the model are derived analytically in the rate-independent case and used to validate the finite element computations performed with the finite element solver Z–set (Besson and Foerch, 1997; Z–set package, 2013).

2.2.1. Geometry and boundary conditions

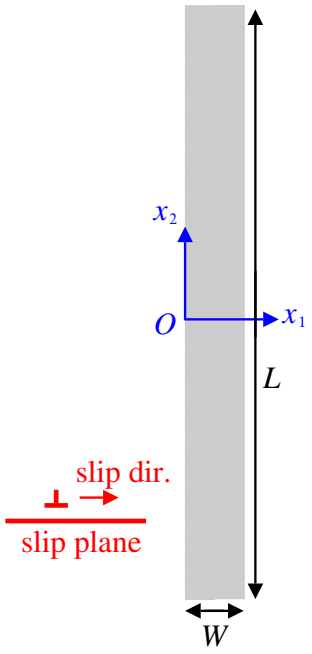

Fig. 2: Periodic unit cell of width W along $\underline{\boldsymbol{X}}_1$, length L along $\underline{\boldsymbol{X}}_2$, and thickness T along $\underline{\boldsymbol{X}}_3$

Let us consider the periodic unit cell of width W in $\underline{\boldsymbol{X}}_1$, length L in $\underline{\boldsymbol{X}}_2$ and thickness T in $\underline{\boldsymbol{X}}_3 = \underline{\boldsymbol{X}}_1 \wedge \underline{\boldsymbol{X}}_2$ directions shown in figure 2. As in (Ling et al., 2018), the problem of simple shear with a unique slip system $(\underline{\boldsymbol{\ell}}, \underline{\boldsymbol{n}})$ aligned with the shearing direction is considered ($\underline{\boldsymbol{\ell}} = \underline{\boldsymbol{X}}_1$ and $\underline{\boldsymbol{n}} = \underline{\boldsymbol{X}}_2$). A macroscopic (average) transformation gradient $\overline{\underline{\underline{\boldsymbol{F}}}}$ is applied such that

$$\underline{\boldsymbol{u}} = (\overline{\underline{\underline{\boldsymbol{F}}}} - \underline{\underline{\mathbf{1}}}).\underline{\boldsymbol{X}} + \underline{\boldsymbol{v}}(\underline{\boldsymbol{X}}), \tag{24}$$

$$\text{with } \overline{\underline{\underline{\boldsymbol{F}}}} = \underline{\underline{\mathbf{1}}} + \overline{F}_{12} \underline{\boldsymbol{\ell}} \otimes \underline{\boldsymbol{n}}, \tag{25}$$

where $\underline{\boldsymbol{v}}$ is a periodic function of periodicity W in $\underline{\boldsymbol{X}}_1$ direction, L in $\underline{\boldsymbol{X}}_2$ direction and T in $\underline{\boldsymbol{X}}_3$ direction. At origin point O zero displacements are imposed in the three directions such that

$$\underline{\boldsymbol{u}}\,(X_1=0,X_2=0,X_3=0)=\underline{\mathbf{0}}\,. \tag{26}$$

In order to enforce existence of gradients of the microslip γ_χ along $\underline{\boldsymbol{X}}_2$ and thus evidence the boundary layer formation, Dirichlet boundary conditions along $\underline{\boldsymbol{X}}_2$ are applied while periodic boundary conditions along $\underline{\boldsymbol{X}}_1$ and $\underline{\boldsymbol{X}}_3$ are considered

$$\begin{aligned}
\gamma_\chi\,(X_1=0,X_2,X_3) &= \gamma_\chi\,(X_1=W,X_2,X_3)\,, &(27)\\
\gamma_\chi\left(X_1,X_2=\pm\frac{L}{2},X_3\right) &= 0, &(28)\\
\gamma_\chi\left(X_1,X_2,X_3=-\frac{T}{2}\right) &= \gamma_\chi\left(X_1,X_2,X_3=\frac{T}{2}\right). &(29)
\end{aligned}$$

Analytical solutions are first obtained in the case of linear hardening ($H>0$) and perfect plasticity ($H=0$) corresponding to the following form of the hardening potential:

$$\rho\psi_h(\gamma_{cum})=\frac{1}{2}\frac{\rho}{\rho_0}H\gamma_{cum}^2, \tag{30}$$

where $\gamma_{cum}=|\gamma|$ in the case of monotonic single slip for which the superscript s is dropped, and H is the hardening modulus. In the reference configuration, the equations that need to be satisfied are the balance laws (7), (8) and yielding condition (22). From (12) one has in simple shear with a single slip system that $\underset{\sim}{\boldsymbol{P}}=\underset{\sim}{\mathbf{1}}+\gamma\underline{\boldsymbol{\ell}}\otimes\underline{\boldsymbol{n}}$. Inspired from the work of (Gurtin, 2000), with $\underset{\sim}{\boldsymbol{F}}=\underset{\sim}{\boldsymbol{E}}.\underset{\sim}{\boldsymbol{P}}$, we make the assumption of small elastic deformations in the absence of lattice rotation expected in the considered slip configuration, i.e $E_{12}\ll 1$ with $\underset{\sim}{\boldsymbol{E}}=\underset{\sim}{\boldsymbol{F}}.\underset{\sim}{\boldsymbol{P}}^{-1}=\underset{\sim}{\mathbf{1}}+E_{12}\underline{\boldsymbol{l}}\otimes\underline{\boldsymbol{n}}$. Hence one obtains:

$$\underset{\sim}{\boldsymbol{E}}^e_{GL} \simeq \frac{E_{12}}{2}\left(\underline{\boldsymbol{l}}\otimes\underline{\boldsymbol{n}}+\underline{\boldsymbol{n}}\otimes\underline{\boldsymbol{l}}\right), \tag{31}$$

and also $\underset{\sim}{\boldsymbol{\Pi}}^e=\underset{\approx}{\boldsymbol{C}}:\underset{\sim}{\boldsymbol{E}}^e_{GL}\simeq\Pi^e_{12}\left(\underline{\boldsymbol{l}}\otimes\underline{\boldsymbol{n}}+\underline{\boldsymbol{n}}\otimes\underline{\boldsymbol{l}}\right)$ where $\underset{\approx}{\boldsymbol{C}}$ is the elasticity tensor. It follows from the definition of Mandel's stress $\underset{\sim}{\boldsymbol{\Pi}}^M=\underset{\sim}{\boldsymbol{E}}^T.\underset{\sim}{\boldsymbol{E}}.\underset{\sim}{\boldsymbol{\Pi}}^e$ and the small elastic strain assumption that $\underset{\sim}{\boldsymbol{\Pi}}^M\simeq\underset{\sim}{\boldsymbol{\Pi}}^e$, and thus, dropping the superscript for the unique system s, one has

$$\tau=\underset{\sim}{\boldsymbol{\Pi}}^M:(\underline{\boldsymbol{\ell}}\otimes\underline{\boldsymbol{n}})\simeq\underset{\sim}{\boldsymbol{\Pi}}^e:(\underline{\boldsymbol{\ell}}\otimes\underline{\boldsymbol{n}}). \tag{32}$$

Hence one obtains $\Pi^e_{12}\simeq\tau$. The assumption of small elastic deformations yields also $\underset{\sim}{\boldsymbol{S}}\simeq\underset{\sim}{\boldsymbol{\Pi}}^e.\underset{\sim}{\boldsymbol{P}}^{-T}$. Note that $\underset{\sim}{\boldsymbol{P}}$ is of the form $\underset{\sim}{\boldsymbol{P}}=\underset{\sim}{\mathbf{1}}+\gamma\underline{\boldsymbol{\ell}}\otimes\underline{\boldsymbol{n}}$, hence $\underset{\sim}{\boldsymbol{P}}^{-T}=\underset{\sim}{\mathbf{1}}-\gamma\underline{\boldsymbol{n}}\otimes\underline{\boldsymbol{\ell}}$ and the balance equation (7) rewrites

$$\mathrm{Div}\left(\underset{\sim}{\boldsymbol{\Pi}}^e-\gamma\underset{\sim}{\boldsymbol{\Pi}}^e.(\underline{\boldsymbol{n}}\otimes\underline{\boldsymbol{\ell}})\right)=\underline{\mathbf{0}}\,, \tag{33}$$

which yield, when projected along $\underline{\boldsymbol{X}}_1$ and $\underline{\boldsymbol{X}}_2$

$$\begin{aligned}
\frac{\partial\tau}{\partial X_2}-\frac{\partial(\gamma\tau)}{\partial X_1} &= 0, &(34)\\
\frac{\partial\tau}{\partial X_2} &= 0. &(35)
\end{aligned}$$

From the periodic boundary conditions (27) and (29), and arbitrariness of the width W and thickness T, invariant solutions along $\underline{\boldsymbol{X}}_1$ and $\underline{\boldsymbol{X}}_3$ will be sought, i.e. $\gamma_\chi(X_1, X_2, X_3) = \gamma_\chi(X_2)$. Similarly, from (17) γ is also invariant along $\underline{\boldsymbol{X}}_1$ and $\underline{\boldsymbol{X}}_3$. As a consequence equation (34) and (35) give respectively that τ is invariant along $\underline{\boldsymbol{X}}_1$ and $\underline{\boldsymbol{X}}_2$. Since the periodic unit cell can be considered arbitrarily thin along $\underline{\boldsymbol{X}}_3$ without loss of generality, τ is also invariant along $\underline{\boldsymbol{X}}_3$. Hence τ is uniform in the periodic unit cell:

$$\tau(X_1, X_2, X_3) = \tau. \tag{36}$$

Combining (19) and (20) with (8) leads to the differential equation governing the microslip

$$A\frac{\mathrm{d}^2\gamma_\chi}{\mathrm{d}X_2^2} = H_\chi(\gamma_\chi - \gamma). \tag{37}$$

From the homogeneity of the shear stress in the unit cell, when yielding occurs the whole unit cell becomes plastic and the yield condition (22) leads to $f = |\tau| - (\tau_0 + H\gamma + H_\chi(\gamma - \gamma_\chi)) = 0$. Combined with (37) one obtains another form of the differential equation governing the microslip

$$A\frac{\mathrm{d}^2\gamma_\chi}{\mathrm{d}X_2^2} - \frac{HH_\chi}{H + H_\chi}\gamma_\chi + \frac{H_\chi}{H + H_\chi}(|\tau| - \tau_0) = 0. \tag{38}$$

Since the shear stress τ is uniform in the unit cell, the differential equation (38) governing the microslip is a second-order, linear, in-homogeneous differential equation with constant coefficients. It is elliptic if $H > 0$ and parabolic if $H = 0$.

2.2.2. Linear hardening ($H > 0$)

In the case of linear hardening Eq. (38) takes the form

$$\frac{\mathrm{d}^2\gamma_\chi}{\mathrm{d}X_2^2} - \left(\frac{2\pi}{\lambda_0}\right)^2 \gamma_\chi \quad = \quad -\left(\frac{2\pi}{\lambda_0}\right)^2 \kappa, \tag{39}$$

where λ_0 and κ are constants defined by:

$$\lambda_0 \quad = \quad 2\pi\sqrt{\frac{A(H + H_\chi)}{|H|H_\chi}}, \text{ assuming } H + H_\chi \geq 0 \tag{40}$$

$$\kappa \quad = \quad \left(\frac{\lambda_0}{2\pi}\right)^2 \frac{H_\chi(|\tau| - \tau_0)}{A(H + H_\chi)}. \tag{41}$$

Note that for large values of the penalty parameter H_χ, one has $H_\chi \gg H$ and the intrinsic length $\lambda_0 \simeq 2\pi\sqrt{A/H}$, which is the expression for the strain gradient plasticity model. For a strictly positive linear hardening, the solutions of (39) are of the form

$$\gamma_\chi(X_2) = \alpha\cosh\left(2\pi\frac{X_2}{\lambda_0}\right) + \beta\sinh\left(-2\pi\frac{X_2}{\lambda_0}\right) + \kappa, \tag{42}$$

where α and β are integration constants. For symmetry reasons $\gamma_\chi(X_2) = \gamma_\chi(-X_2)$ which leads to $\beta = 0$ and α is uniquely determined from boundary condition (28):

$$\alpha = -\frac{\kappa}{\cosh\left(\frac{2\pi}{\lambda_0}\frac{L}{2}\right)}, \tag{43}$$

which finally leads to

$$\gamma_\chi = \kappa \left(1 - \frac{\cosh\left(\frac{2\pi}{\lambda_0} X_2\right)}{\cosh\left(\frac{2\pi}{\lambda_0}\frac{L}{2}\right)} \right). \tag{44}$$

Since $\underset{\sim}{\boldsymbol{F}} = \underset{\sim}{\boldsymbol{E}}.\underset{\sim}{\boldsymbol{P}} = (\underset{\sim}{\mathbf{1}} + E_{12}(\underline{\boldsymbol{l}} \otimes \underline{\boldsymbol{n}})).(\underset{\sim}{\mathbf{1}} + \gamma(\underline{\boldsymbol{l}} \otimes \underline{\boldsymbol{n}})) \simeq (\underset{\sim}{\mathbf{1}} + (E_{12} + \gamma)(\underline{\boldsymbol{l}} \otimes \underline{\boldsymbol{n}}))$ from (31) and (36) one has

$$\tau = \Pi^e_{12} = 2C_{44} E^e_{GL,12} = \frac{2C_{44}}{L} \int_{-\frac{L}{2}}^{\frac{L}{2}} \left(\frac{F_{12} - \gamma}{2} \right) \mathrm{d}X_2, \tag{45}$$

where C_{44} denotes the elastic shear modulus. From yielding condition (22) γ can be replaced by $\frac{|\tau| - \tau_0 + H_\chi \gamma_\chi}{H + H_\chi}$ in (45) and the integration provides an expression of τ as a function of the applied macroscopic (average) shear $\overline{F}_{12}$ and material parameters:

$$\tau = \frac{\overline{F}_{12} + \frac{\tau_0}{Z_h}}{\frac{1}{C_{44}} + \frac{1}{Z_h}}, \tag{46}$$

$$\text{where } \frac{1}{Z_h} = \frac{1}{H} - \frac{2H_\chi \tanh\left(\frac{2\pi}{\lambda_0}\frac{L}{2}\right)}{L\frac{2\pi}{\lambda_0} H(H + H_\chi)}. \tag{47}$$

2.2.3. Perfect plasticity ($H = 0$)

For the case of perfect plasticity, $H = 0$, the same periodic and Dirichlet type boundary value problem as in the previous section is studied. In that case the differential equation (38) becomes

$$\frac{\mathrm{d}^2 \gamma_\chi}{\mathrm{d}X_2^2} + \frac{|\tau| - \tau_0}{A} = 0. \tag{48}$$

The analytical reference solution in case of perfect plasticity is thus of polynomial form

$$\gamma_\chi(X_2) = \frac{\tau_0 - |\tau|}{2A} X_2^2 + \alpha X_2 + \beta, \tag{49}$$

where α and β are integration constants, which are uniquely determined from boundary conditions

$$\alpha = 0 \quad \text{and} \quad \beta = -\frac{\tau_0 - |\tau|}{8A} L^2, \tag{50}$$

which finally leads to

$$\gamma_\chi(X_2) = \frac{\tau_0 - |\tau|}{2A} \left(X_2^2 - \left(\frac{L}{2}\right)^2 \right). \tag{51}$$

This solution is also obtained when computing the Taylor expansion at order two of (44) with H going to zero, i.e λ_0 going to infinity and X_2/λ_0 going to 0. Using the uniformity of the shear stress in the unit cell, equation (45) leads now to

$$\tau = \frac{\overline{F}_{12} + \frac{\tau_0}{Z_p}}{\frac{1}{C_{44}} + \frac{1}{Z_p}}, \tag{52}$$

$$\text{where } \frac{1}{Z_p} = \frac{1}{H_\chi} + \frac{L^2}{12A}, \tag{53}$$

which is also obtained with the Taylor expansion of (47) when H goes to zero. In the case of strictly positive linear hardening a boundary layer solution is obtained. The size of the boundary layer depends

Table 1: Numerical values of material and unit cell parameters.

C_{11}	C_{12}	C_{44}	τ_0	A	H_χ	n	$\dot{\gamma}_0$	L
200 GPa	136 GPa	105 GPa	10 MPa	1 N	10^5 MPa	15	$10^{17}\,\mathrm{s}^{-1}$	1 mm

on the ratio between the material length scale λ_0 and the size L of the unit cell. In the case of perfect plasticity, it appears that the size of the plastic zone, or in other words the radius of curvature of the parabola, depends not only on the higher order modulus A but also on the size L of the unit cell.

The analytical solutions (44) and (51) are used to validate the finite element solution of the same boundary value problem. The unit cell is discretized regularly in 101 elements (reduced integration with eight Gauss points). The interpolation is quadratic for the displacements $\underline{\boldsymbol{u}}$ and linear for γ_χ. Cubic elasticity is considered and C_{11}, C_{12} and C_{44} denote the elasticity moduli. Table 1 gathers the material parameters that have been used for validation in case of linear hardening $H = 1000\,\mathrm{MPa}$ and perfect plasticity $H = 0\,\mathrm{MPa}$. Figure 3 shows the finite element and analytical solutions at $\overline{F}_{12} = 1\%$. Viscosity parameters $\dot{\gamma}_0$ and n have been chosen such that the response is almost rate-independent. The viscous part of the stress is equal to $\tau_0(\dot{\gamma}/\dot{\gamma}_0)^{1/n}$. With the chosen values of the parameters, it is more than 20 times lower than the critical resolved shear stress in the range of strain rates considered here. A perfect agreement is also obtained for any other value of $\overline{F}_{12}$.

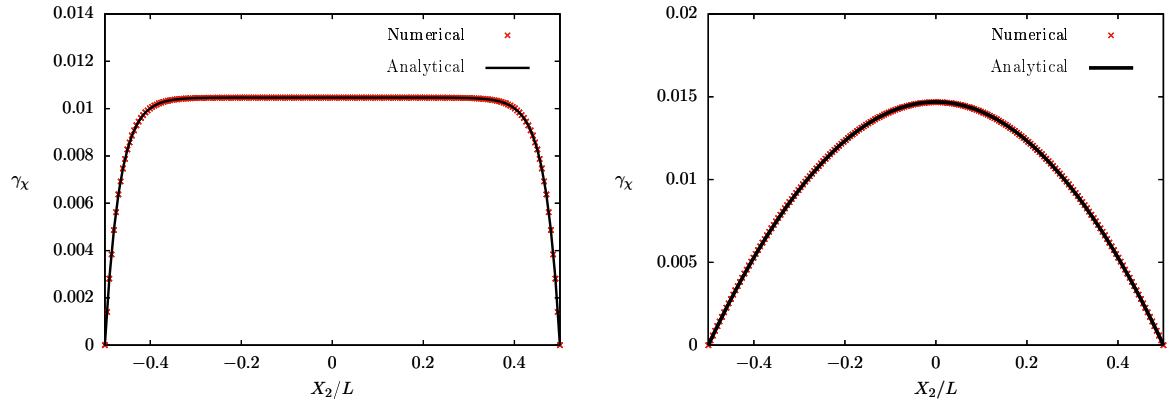

Fig. 3: Analytical (black line) and finite element (red crosses) solutions of differential equation (38) with: (a) a strictly positive linear hardening ($H = 1000\,\mathrm{MPa}$) and (b) perfect plasticity ($H = 0\,\mathrm{MPa}$) at $\overline{F}_{12} = 1\%$

3. Simple shear in the case of softening behaviour

This section is dedicated to the prediction of the micromorphic crystal plasticity model for softening behaviour and in particular to the formation of localization slip bands. As mentioned in the introduction strain gradient models can be used to regularize strain localization phenomena by introducing one or several characteristic lengths. It is shown here how the model presented in section

2 incorporates an intrinsic length that, in case of single slip and linear softening, is related to the localization slip band width. Then non-linear saturating softening behaviour are shown to trigger an increasing slip localization band width. An enhanced model is then proposed in order to bound the localization band width and thus confine the localization zone when the softening behaviour tends toward perfect plasticity.

3.1. Linear softening ($H < 0$)

Let us now consider a linear softening behaviour ($H < 0$ in the hardening potential (30)). The same boundary conditions (27), (28) and (29) as in previous section are kept. Because of the material softening a plastic instability is expected. Therefore a solution with localized plastic deformation over a width λ along $\underline{\boldsymbol{X}}_2$ and centered at O is sought for. In the plastic zone the yield condition is satisfied while $\dot{\gamma}$ is zero in the elastic zone

$$f = 0 \qquad \forall X_2 \in \left[-\tfrac{\lambda}{2}; \tfrac{\lambda}{2}\right], \tag{54}$$

$$\dot{\gamma} = 0 \quad \forall X_2 \in \left[-\tfrac{L}{2}; -\tfrac{\lambda}{2}\right] \cup \left[\tfrac{\lambda}{2}; \tfrac{L}{2}\right]. \tag{55}$$

The differential equation (38) governing γ_χ is only valid in the region $X_2 \in \left[-\frac{\lambda}{2}; \frac{\lambda}{2}\right]$ and the solutions are of the form

$$\gamma_\chi(X_2) \quad = \quad \alpha \cos\left(2\pi \frac{X_2}{\lambda_0}\right) + \beta \sin\left(2\pi \frac{X_2}{\lambda_0}\right) + \kappa. \tag{56}$$

For symmetry reasons $\gamma_\chi(X_2) = \gamma_\chi(-X_2)$, hence $\beta = 0$. Out of the plastic zone $\gamma(X_2) = 0$ and at the elastic/plastic interfaces, i.e at $X_2 = \pm\frac{\lambda}{2}$, continuity of microslip γ_χ and of generalized stress normal to the interface $\underline{\boldsymbol{M}}.\underline{\boldsymbol{X}}_2$ must hold, hence

$$\gamma_\chi\left(\pm\frac{\lambda}{2}\right) \simeq \gamma\left(\pm\frac{\lambda}{2}\right) \quad = \quad 0, \tag{57}$$

$$\underline{\boldsymbol{M}}\left(\pm\frac{\lambda}{2}\right).\underline{\boldsymbol{X}}_2 = A\frac{\mathrm{d}\gamma_\chi}{\mathrm{d}X_2}\Big|_{X_2=\pm\frac{\lambda}{2}} \quad = \quad 0. \tag{58}$$

Combining (57) and (58) with (56) one gets

$$\alpha \quad = \quad \frac{|\tau| - \tau_0}{H}, \tag{59}$$

$$\lambda \quad = \quad \lambda_0. \tag{60}$$

Hence it is shown that, for $H_\chi \gg H$, the material parameters H and A fully determine the width $\lambda = \lambda_0 \simeq \sqrt{\frac{A}{H}}$ of the localization slip band that arises in single slip with a linear softening behaviour. This is in contrast to the parabolic case of the previous section for which the plastic zone size depends on the length of the unit cell. From (45) the uniform shear stress writes

$$\tau \quad = \quad \frac{\overline{F}_{12} + \frac{\tau_0}{Z_e}}{\frac{1}{C_{44}} + \frac{1}{Z_e}}, \tag{61}$$

$$\text{where } \frac{1}{Z_e} \quad = \quad \frac{\lambda_0}{HL}. \tag{62}$$

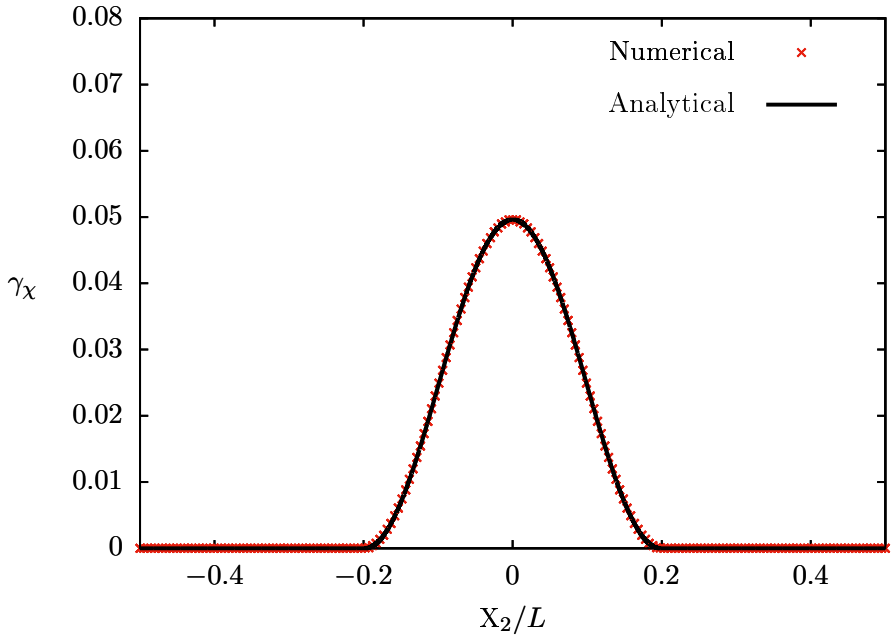

Fig. 4: Analytical (black line) and finite element (red crosses) solutions of differential equation (38) with a linear negative hardening ($H = -250\,\mathrm{MPa}$) at $\overline{F}_{12} = 1\%$

In the case of strictly negative linear softening the localized solution obtained is a cosine profile. The period of the cosine function is a material parameter and it is equal to the width of the localization band. If the length L of the unit cell is larger than λ_0 the period of the cosine function is then equal to L.

Numerically, in order to trigger the localization instability in the center of the periodic unit cell, a defect is introduced in its middle. It consists in a single element having an initially slightly lower critical resolved shear stress τ_0^{defect} taken equal to 99% of τ_0. The analytical solution (56) is used to validate the finite element solution of the same boundary value problem using the same mesh as in section 2. Figure 4 shows both solutions at $\overline{F}_{12} = 1\%$. A perfect agreement is also obtained for any other value of $\overline{F}_{12}$.

3.2. Non-linear softening and localization slip band widening

A linear softening behaviour is useful to establish analytical reference solutions, but is of limited interest for modelling softening in real materials at large deformations. In order to model any given saturating softening behaviour, for example the clearing of Frank dislocation loops inside dislocation channels relevant for irradiated materials, we propose to introduce in (16) a non-linear exponential softening by means of the hardening potential

$$\rho\psi_h = -\frac{\rho}{\rho_0}\tau_a\gamma_0 \exp\left(-\frac{\gamma_{cum}}{\gamma_0}\right). \tag{63}$$

This kind of softening is similar to the phenomenological dislocation unpinning model proposed by Ling et al. (2017). The goal of the present subsection is to evidence the broadening of the localization

band when such a non-linear softening behaviour is adopted inside the formulation presented in section 2. An enhanced model is then proposed in order to bound a priori the localization slip band width when considering linear and non-linear softening behaviours. (Zbib and Aifantis, 1988) evidenced the narrowing of localization shear bands by adopting a concave parabolic hardening. However, parabolic softening is unrealistic at large strains and is not used in the present work. As shown in the previous subsection, for simple shear in single slip, a constant band width is obtained in case of a linear softening. Hence a slip band width widening is expected to occur due to the increase of the (negative) tangent softening modulus of the softening proposed in equation (63). The yield condition (22) in the particular case of a non-linear exponential hardening writes:

$$f^s = |\tau^s| - \left(\tau_0 - H_\chi(\gamma_\chi - \gamma_{cum}) + \tau_a\gamma_0 \exp\left(-\frac{\gamma_{cum}}{\gamma_0}\right)\right) = 0. \tag{64}$$

The solution in terms of γ_{cum} for yielding condition (64) involves the Lambert $\mathcal{W}$ function[2]. Finally γ_{cum} is eliminated from the differential equation (37) which provides

$$A\frac{\mathrm{d}^2\gamma_\chi}{\mathrm{d}X_2^2} + H_\chi\gamma_0\mathcal{W}\left(-\frac{\tau_a}{H_\chi\gamma_0}\exp\left(\frac{\tau_0 - |\tau| - H_\chi\gamma_\chi}{H_\chi\gamma_0}\right)\right) = \tau_0 - |\tau|. \tag{65}$$

This differential equation cannot be solved analytically, however a local analysis in the neighbourhood of a given point $\underline{\boldsymbol{X}} = \underline{\boldsymbol{X}}^0$ suffices to prove the widening of the localization band. The function $\frac{\mathrm{d}\psi_h}{\mathrm{d}\gamma_{cum}}$ is then approximated by its Taylor expansion in $\underline{\boldsymbol{X}}^0$ with

$$\frac{\mathrm{d}\psi_h}{\mathrm{d}\gamma_{cum}}(\gamma_{cum}) \simeq H_T^0(\gamma_{cum} - \gamma_{cum}(X_2^0)) + \frac{\mathrm{d}\psi_h}{\mathrm{d}\gamma_{cum}}(\gamma_{cum}(X_2^0)), \tag{66}$$

$$\text{with } H_T^0 = \frac{\mathrm{d}^2\psi_h}{\mathrm{d}\gamma_{cum}^2}(\gamma_{cum}(X_2^0)). \tag{67}$$

This expression can be substituted in (22) and the same analysis as in previous subsection leads then to a local characteristic length scale λ which is similar to the case of linear softening

$$\lambda = 2\pi\sqrt{\frac{A(H_T^0 + H_\chi)}{|H_T^0|H_\chi}} \simeq 2\pi\sqrt{\frac{A}{|H_T^0|}}. \tag{68}$$

$|H_T^0|$ decreases when $\gamma_{cum}(X_2^0)$ increases and ranges in $\left]0; \frac{\tau_a}{\gamma_0}\right]$. γ_{cum} reaches its maximum at the center of the defect ($X_2^0 = 0$), so λ is maximum at $X_2^0 = 0$ and goes to infinity when softening saturates, i.e. when $\gamma_{cum}(X_2^0)$ goes to infinity and $|H_T^0|$ goes to 0. Finally this proves that the localization band width tends to increase when increasing $\overline{F}_{12}$. This result has been verified by computing the finite element solution of the γ_χ profile for the exponential softening potential (63). Figure 5 shows the numerical solution obtained for different values of $\overline{F}_{12}$. Eventually for large values of γ_{cum} the localization slip band edges reach the boundary of the periodic unit cell and plastic deformation tends to become homogeneous. This feature of localization slip band broadening is not acceptable when trying to simulate continuing localization at plastic strains much greater than the softening saturating strain ($\gamma_{cum} \gg \gamma_0$).

[2]For $z \in \mathbb{C}$, and the function $f : z \mapsto ze^z$, the Lambert $\mathcal{W}$ function is defined as the inverse function of f, i.e such that for $z \in \mathbb{C}$, $z = f^{-1}(ze^z) = \mathcal{W}(ze^z)$

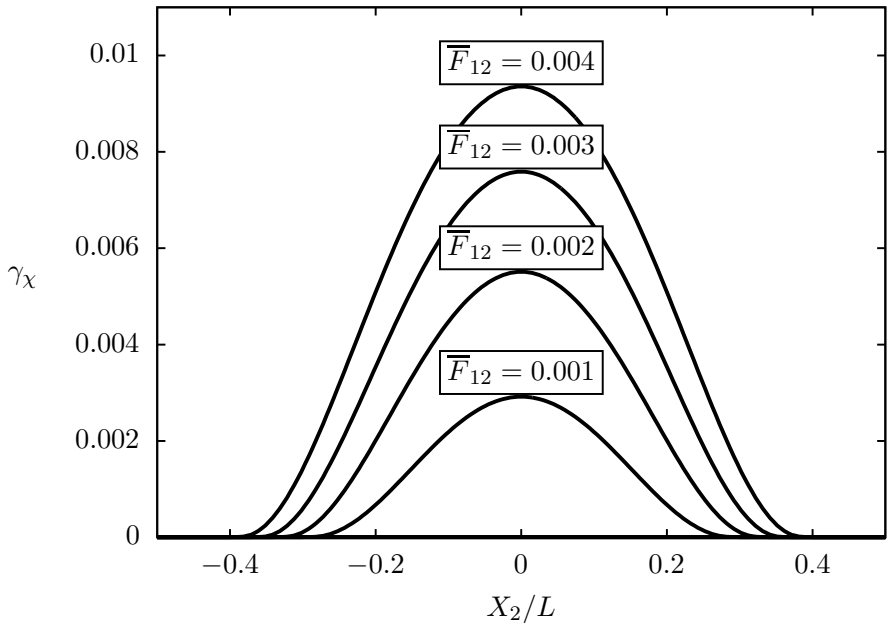

Fig. 5: Finite element solution of equation (37) for an exponential softening behaviour displaying localization band width widening

3.3. An enhanced model for a bounded localization slip band width

An enhanced micromorphic crystal plasticity model is therefore proposed in order to bound a priori the localization slip band width when solving the problem of simple shear in single slip. Up to now A was taken as a constant material parameter, while hardening was taken into account with the hardening potential $\psi_h(\gamma_{cum})$. Here a dependence of the higher order modulus A with respect to γ_{cum} is introduced in the form:

$$A(\gamma_{cum}) \quad = \quad -\left(\frac{\Lambda_0}{2\pi}\right)^2 \rho_\sharp \frac{\mathrm{d}^2\psi_h}{\mathrm{d}\gamma_{cum}^2}, \tag{69}$$

where Λ_0 has the dimension of a length. The corresponding Lagrangian potential (16) writes:

$$\rho\psi = \frac{1}{2}\frac{\rho}{\rho_\sharp}\underset{\sim}{\boldsymbol{E}}^e_{GL} : \underset{\approx}{\boldsymbol{C}} : \underset{\sim}{\boldsymbol{E}}^e_{GL} + \frac{1}{2}\frac{\rho}{\rho_0}H_\chi e^2 + \frac{1}{2}\frac{\rho}{\rho_0}A(\gamma_{cum})\underline{\boldsymbol{K}}^T.\underline{\boldsymbol{K}} + \rho\psi_h(\gamma_{cum}). \tag{70}$$

By virtue of the second law of thermodynamics the state laws (18) and (19) still hold and (20) becomes

$$\underline{\boldsymbol{M}} \quad = \quad A(\gamma_{cum})\underline{\boldsymbol{K}}\,. \tag{71}$$

The residual dissipation inequality is now

$$\sum_{s=1}^{N}\left(|\tau^s| + \frac{\rho_\sharp}{\rho}s - \rho_\sharp\frac{\mathrm{d}\psi_h}{\mathrm{d}\gamma_{cum}} - \frac{1}{2}\frac{\mathrm{d}A}{\mathrm{d}\gamma_{cum}}\underline{\boldsymbol{K}}^T.\underline{\boldsymbol{K}}\right)|\dot{\gamma}^s| \geqslant 0. \tag{72}$$

An enhanced yield function is proposed in the form

$$f^s = |\tau^s| - \left(\tau_0 - \frac{\rho_\sharp}{\rho}s + \rho_\sharp\frac{\mathrm{d}\psi_h}{\mathrm{d}\gamma_{cum}} + \frac{1}{2}\frac{\mathrm{d}A}{\mathrm{d}\gamma_{cum}}\underline{\boldsymbol{K}}^T.\underline{\boldsymbol{K}}\right). \tag{73}$$

It can be seen that the introduction of an evolving higher order modulus induces additional apparent hardening in the expression of the effective critical resolved shear stress. For the problem of single slip considered here superscript s is dropped and combining (71) with the balance equation (8) and yielding condition (73) one obtains the general differential equation inside the plastic zone $[-\frac{\lambda}{2};\frac{\lambda}{2}]$

$$A(\gamma_{cum})\frac{\mathrm{d}^2\gamma_\chi}{\mathrm{d}X_2^2} = \frac{1}{2}\frac{\mathrm{d}A}{\mathrm{d}\gamma_{cum}}\left(\frac{\mathrm{d}\gamma_\chi}{\mathrm{d}X_2}\right)^2 - \frac{\mathrm{d}A}{\mathrm{d}\gamma_{cum}}\frac{\mathrm{d}\gamma_{cum}}{\mathrm{d}X_2}\frac{\mathrm{d}\gamma_\chi}{\mathrm{d}X_2} + \tau_0 + \rho_\sharp\frac{\mathrm{d}\psi_h}{\mathrm{d}\gamma_{cum}} - |\tau|. \tag{74}$$

At this step it is straightforward to show that (73) and (74) reduce respectively to (22) and (39) in case of a linear hardening/softening behaviour ($\psi_h(\gamma_{cum}) = \frac{1}{2}H\gamma_{cum}^2$). In that case $\Lambda_0 = \lambda$ and the solutions of this equation have been detailed in sections 2.2.2, 2.2.3 and 3.1. For an exponential softening behaviour of the type proposed in (63) one has

$$\rho_\sharp\frac{\mathrm{d}\psi_h}{\mathrm{d}\gamma_{cum}} = \tau_a\exp\left(-\frac{\gamma_{cum}}{\gamma_0}\right) \quad \text{and} \quad A(\gamma_{cum}) = \left(\frac{\Lambda_0}{2\pi}\right)^2\frac{\tau_a}{\gamma_0}\exp\left(-\frac{\gamma_{cum}}{\gamma_0}\right). \tag{75}$$

Note that $A(\gamma_{cum}) \geq 0$ such that the free energy potential is convex with respect to the microslip gradient. Two approximations allow us to derive an approximate closed form solution to differential equation (74).

Approximation 1

At initiation of plastic slip, gradients along $\underline{\boldsymbol{X}}_2$ of cumulated plastic slip and microslip are close to zero. Therefore we propose to neglect the first and second terms of the right-hand side of differential equation (74) that involve quadratic terms of these gradients. The approximate differential equation becomes

$$A(\gamma_{cum})\frac{\mathrm{d}^2\gamma_\chi}{\mathrm{d}X_2^2} = \tau_0 + \rho_\sharp\frac{\mathrm{d}\psi_h}{\mathrm{d}\gamma_{cum}} - |\tau|. \tag{76}$$

Approximation 2

The analytical solutions are derived in the limit case of SGCP, i.e. when the penalty factor H_χ of the micromorphic model is large enough. Therefore combining (75) with approximated differential equation (76) and approximations (17), one gets

$$\left(\frac{\Lambda_0}{2\pi}\right)^2\frac{\tau_a}{\gamma_0}\exp\left(-\frac{\gamma_{cum}}{\gamma_0}\right)\frac{\mathrm{d}^2\gamma_{cum}}{\mathrm{d}X_2^2} = \tau_0 + \tau_a\exp\left(-\frac{\gamma_{cum}}{\gamma_0}\right) - |\tau|. \tag{77}$$

With the variable substitution

$$\Gamma = \exp\left(-\frac{\gamma_{cum}}{\gamma_0}\right), \tag{78}$$

the derivatives with respect to X_2 are rewritten as

$$\frac{\mathrm{d}\Gamma}{\mathrm{d}X_2} = -\frac{1}{\gamma_0}\exp\left(-\frac{\gamma_{cum}}{\gamma_0}\right)\frac{\mathrm{d}\gamma_{cum}}{\mathrm{d}X_2}, \tag{79}$$

$$\text{and } \frac{\mathrm{d}^2\Gamma}{\mathrm{d}X_2^2} = \frac{1}{\gamma_0^2}\exp\left(-\frac{\gamma_{cum}}{\gamma_0}\right)\left(\frac{\mathrm{d}\gamma_{cum}}{\mathrm{d}X_2}\right)^2 - \frac{1}{\gamma_0}\exp\left(-\frac{\gamma_{cum}}{\gamma_0}\right)\frac{\mathrm{d}^2\gamma_{cum}}{\mathrm{d}X_2^2} \tag{80}$$

$$\simeq -\frac{1}{\gamma_0}\exp\left(-\frac{\gamma_{cum}}{\gamma_0}\right)\frac{\mathrm{d}^2\gamma_{cum}}{\mathrm{d}X_2^2}. \tag{81}$$

where quadratic terms of the gradient of cumulated plastic slip are again neglected. The differential equation governing Γ is then derived from Eq. (77) as

$$\frac{\mathrm{d}^2\Gamma}{\mathrm{d}X_2^2} + \left(\frac{2\pi}{\Lambda_0}\right)^2 \Gamma = \left(\frac{2\pi}{\Lambda_0}\right)^2 \frac{|\tau| - \tau_0}{\tau_a}. \tag{82}$$

Its solutions are of the form

$$\Gamma(X_2) \quad = \quad \alpha \cos\left(2\pi\frac{X_2}{\Lambda_0}\right) + \beta \sin\left(2\pi\frac{X_2}{\Lambda_0}\right) + \frac{|\tau| - \tau_0}{\tau_a}, \tag{83}$$

where α and β are integration constants. Inserting the latter result into the yield condition $f = 0$ one has

$$\gamma_\chi(X_2) = \frac{\tau_0 - |\tau|}{H_\chi} + \frac{\tau_a}{H_\chi}\Gamma(X_2) - \gamma_0 \ln(\Gamma(X_2)). \tag{84}$$

For symmetry reasons $\gamma_\chi(X_2) = \gamma_\chi(-X_2)$, hence $\beta = 0$. Combining (57) and (58) one obtains

$$\lambda \quad = \quad \Lambda_0, \tag{85}$$

$$\alpha \quad = \quad \frac{|\tau| - (\tau_0 + \tau_a)}{\tau_a}. \tag{86}$$

The approximated analytical solution (84) is compared to the finite element solution of the same boundary value problem using the full model and using the same mesh as in section 2. Figure 6 shows both solutions at $\overline{F}_{12} = 0.05\%$ and $\overline{F}_{12} = 0.1\%$. Since approximation 1 is only valid close to initiation of plastic slip, agreement between analytical and numerical results deteriorates when $\overline{F}_{12}$ increases. Nevertheless one should notice that close to the elastic/plastic interfaces a good agreement is obtained because gradients of cumulated plastic slip and microslip remain small in these regions. As a consequence the width of the localization zone obtained numerically remains bounded and close to the one derived analytically and given by (85). Figure 7 displays in dashed lines the finite element solution obtained with the expression of $A(\gamma_{cum})$ expressed at (69) in case of an exponential softening for different values of $\overline{F}_{12}$ ($\overline{F}_{12} \in \{0.001, 0.002, 0.003, 0.004\}$). The solid curves on figure 7 are the one plotted in figure 5 used to show localization band widening when a constant value of A is taken.

The proposed expression of $A(\gamma_{cum})$ allows to bound the localization band width at any strain when considering an exponential softening[3]. However it can be observed from figure 7 that while the size of the region where plastic slip occured is fixed, the size of the region of continuing plastic flow decreases for further straining $\overline{F}_{12}$. The latter region becomes vanishingly thin since its size is proportional to the square root of higher order modulus A which, according to Eq. (75), tends to zero for increasing plastic slip. This means that the classical crystal plasticity model, without regularization, is retrieved. To that extent, the band width becomes close to the mesh size in the finite element simulation.

[3]Results not shown here indicate that a bounded localization band width is obtained also when considering a bi-linear (softening followed by a plateau) behaviour.

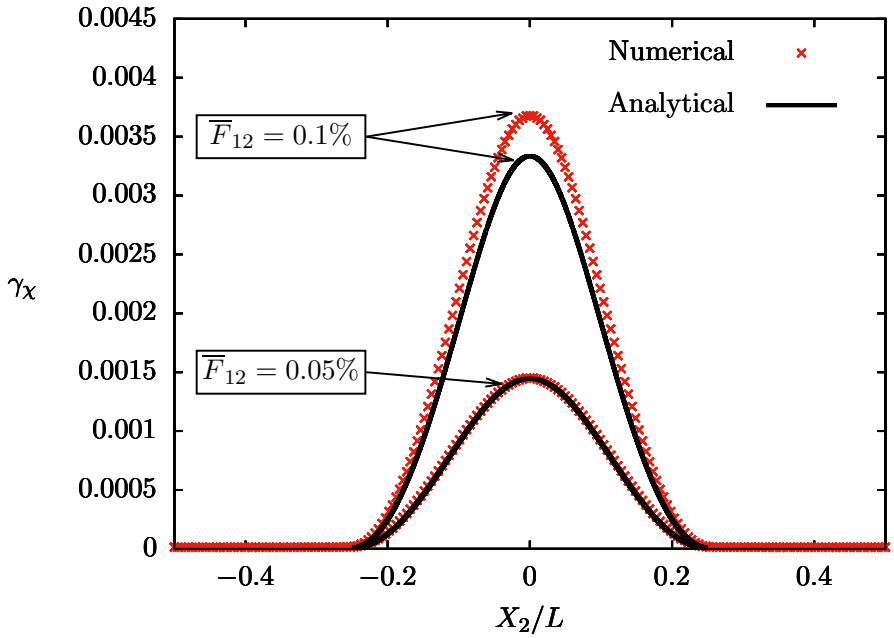

Fig. 6: Analytical (black line) and finite element (red crosses) solutions of differential equation governing γ_χ at $\overline{F}_{12} = 0.05\%$ and $\overline{F}_{12} = 0.1\%$, when considering the non-linear softening behaviour (63) and the constitutive function (69) for $A(\gamma_{cum})$

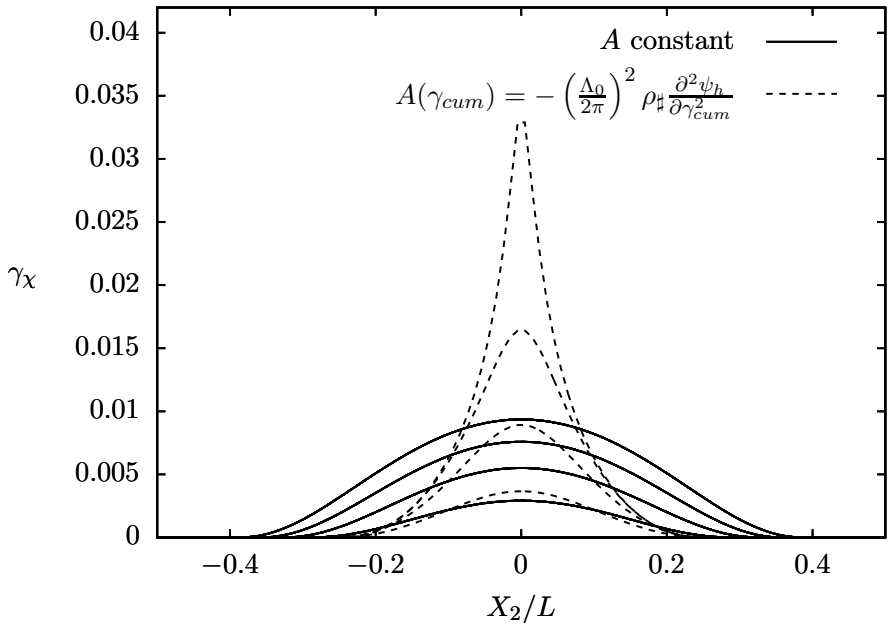

Fig. 7: Finite element solutions of differential equation governing γ_χ for A constant displaying localization band width widening (solid line) and for $A(\gamma_{cum})$ inducing a bounded localization band width (dashed line)

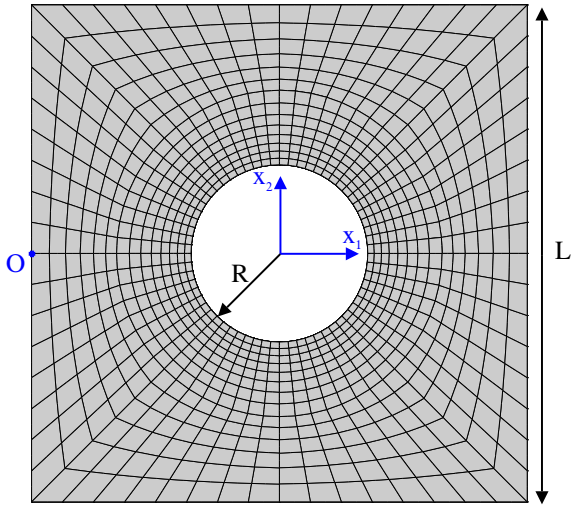

Fig. 8: Periodic unit cell mesh with a cylindrical hole (width and height L and thickness T)

4. Application to irradiated voided crystals: void/slip band interaction

As shown in (Fish et al., 1973) and on figure 1b, irradiation induced nanovoids may be heavily sheared inside dislocation channels during straining. The objective here is to study the possible interactions between these voids and such localization bands from a continuum mechanical perspective. It is shown experimentally in (Farrell et al., 2003) and numerically in (Cui et al., 2018) that essentially one single slip system is active inside such a dislocation channel. Therefore a single slip system is considered in the following. A periodic distribution of voids in a plate is considered for simplicity. Interactions between voids and localization bands are analyzed in the finite element simulation of a single unit cell with appropriate periodic boundary conditions.

4.1. Finite element meshes, loading and boundary conditions

The periodic unit cell is made of a one-element thick square plate of width and height L in direction $\underline{\boldsymbol{X}}_1$ and $\underline{\boldsymbol{X}}_2$ and thickness T along $\underline{\boldsymbol{X}}_3$. A cylindrical hole of radius R is located at the center. Regular meshes consist of hexahedral elements which are quadratic in displacements $\underline{\boldsymbol{u}}$ and linear in γ_χ (reduced integration with eight integration points). In the same way as in previous section, an average deformation gradient $\overline{F}_{12}$ is prescribed to the unit cell with fully periodic boundary conditions. This corresponds to the same macroscopic simple glide deformation field (25) as in the previous section. The microslip variable γ_χ is taken periodic along all three directions. A unique slip system $(\underline{\boldsymbol{\ell}}, \underline{\boldsymbol{n}})$ aligned with the shearing direction 1 is considered ($\underline{\boldsymbol{\ell}} = \underline{\boldsymbol{X}}_1$ and $\underline{\boldsymbol{n}} = \underline{\boldsymbol{X}}_2$). An exponential softening behaviour of type (63) is used and equation (69), and more precisely (75), are adopted for the evolution of the higher order modulus $A(\gamma_{cum})$. Cubic elasticity is considered and table 2 gathers the numerical values of fixed material parameters used for all the simulations.

Table 2: Numerical values of material parameters for the simulation of periodic porous unit cells

C_{11}	C_{12}	C_{44}	τ_0	τ_a	γ_0	Λ_0	H_χ	n	$\dot{\gamma_0}$
200 GPa	136 GPa	105 GPa	235 MPa	35 MPa	0.1	100 nm	10^6 MPa	15	$10^{20}\,\mathrm{s}^{-1}$

Table 3: Discrete values of parameters of interest in the simulation of slip band/void interactions

$\chi_0 = 2R/L$	$q_0 = R/\Lambda_0$
$[0.2, 0.4]$	$[1/18, 1/12, 1/9, 1/6, 1/3]$

4.2. Choice of geometrical and material parameters

The initial void volume fraction is defined as

$$f_0^{\text{band}} = \frac{\pi R^2 T}{2RLT} = \frac{\pi R}{2L}, \tag{87}$$

which represents the ratio between the volume of the cylindrical hole to the volume of the box of edge length L along $\underline{\boldsymbol{X}}_1$ and $2R$ along $\underline{\boldsymbol{X}}_2$ as plasticity is expected to localize in that region. In fact this void volume fraction is proportional to the intervoid spacing ratio χ_0 defined as

$$\chi_0 \quad = \quad \frac{2R}{L}. \tag{88}$$

The ratio q_0 of the intrinsic length to void size is defined as

$$q_0 \quad = \quad \frac{R}{\Lambda_0}. \tag{89}$$

where the constitutive intrinsic length Λ_0 enters Eq. (69). For convenience purposes in the following χ_0 will referred to as the porosity and q_0 as the normalized void size.

Throughout all simulations Λ_0 is fixed to 100 nm which corresponds to an upper bound of the dislocation channels width observed in irradiated steels. Noting that according to (Farrell et al., 2003), the greater the irradiation dose the wider and the fewer the dislocation channels. Such a size is at the limit of continuum mechanical modeling. It is therefore assumed that there are enough dislocation sources in these bands for strain gradient continuum crystal plasticity to be applicable. Table 3 gathers the discrete values retained for the parameters χ_0 and q_0 in the following simulations.

4.3. Results

Figure 9 shows the results obtained for a macroscopic shear strain $\overline{F}_{12} = 0.15$. Very large strains are reached inside the localization band in accordance with the large deformation setting of the theory and finite element implementation. It is important to note that local strains may significantly exceed the maximum value of the cumulated plastic strain γ_{cum} of the legend bar. Also for visualization purposes all unit cells are displayed with the same size for a given void volume fraction, even though the actual hole and cell sizes are varied.

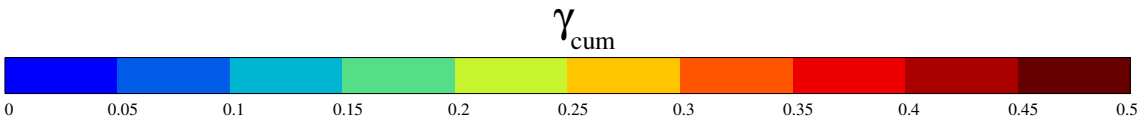

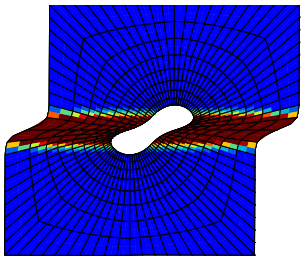

(a) $\chi_0 = 0.2$ and $q_0 = 1/3$

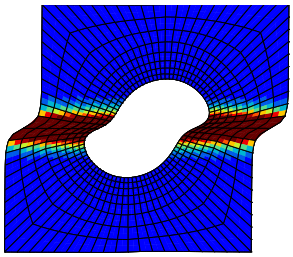

(b) $\chi_0 = 0.4$ and $q_0 = 1/3$

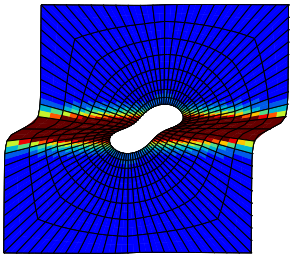

(c) $\chi_0 = 0.2$ and $q_0 = 1/6$

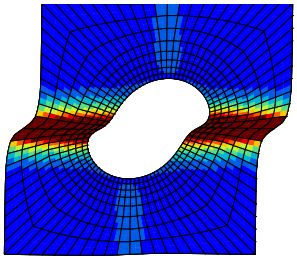

(d) $\chi_0 = 0.4$ and $q_0 = 1/6$

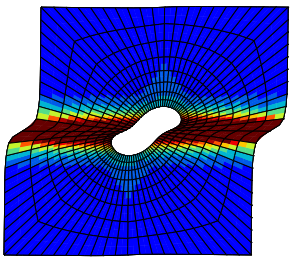

(e) $\chi_0 = 0.2$ and $q_0 = 1/9$

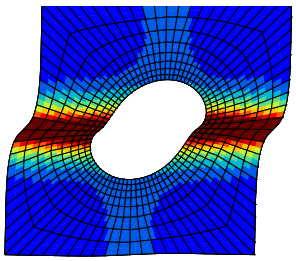

(f) $\chi_0 = 0.4$ and $q_0 = 1/9$

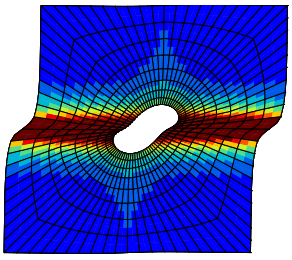

(g) $\chi_0 = 0.2$ and $q_0 = 1/12$

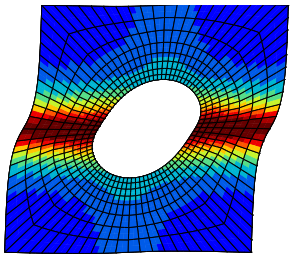

(h) $\chi_0 = 0.4$ and $q_0 = 1/12$

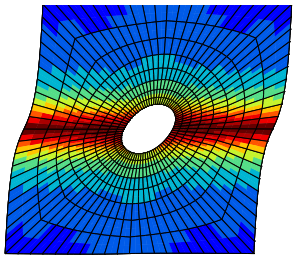

(i) $\chi_0 = 0.2$ and $q_0 = 1/18$

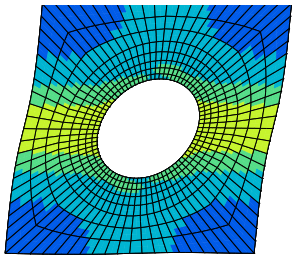

(j) $\chi_0 = 0.4$ and $q_0 = 1/18$

Fig. 9: Finite element results showing the interaction of a slip band and a void in a unit cell under average shear at $\overline{F}_{12} = 0.15$

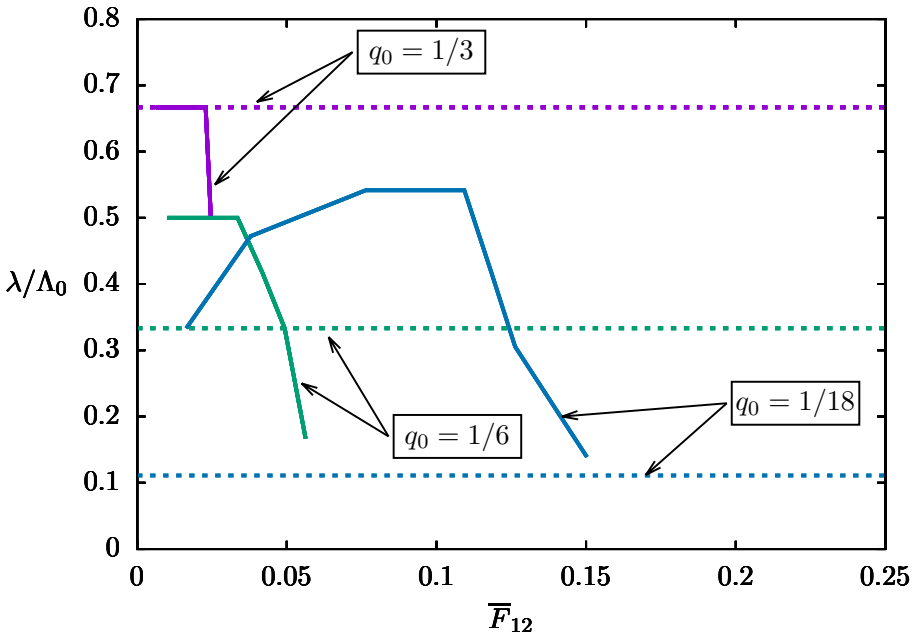

Fig. 10: Normalized localization slip band width λ as a function of $\overline{F}_{12}$ for three different values of parameter q_0 and for $\chi_0 = 0.2$. Dashed lines represent the normalized width equal to four times the initial mesh size.

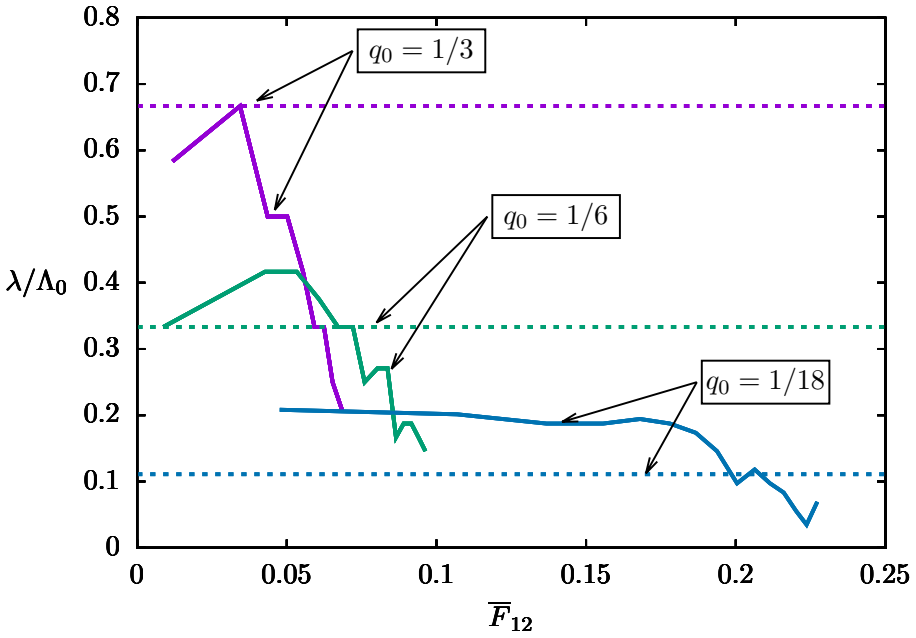

Fig. 11: Normalized localization slip band width λ as a function of $\overline{F}_{12}$ for three different values of parameter q_0 and for $\chi_0 = 0.4$. Dashed lines represent the normalized width equal to four times the initial mesh size.

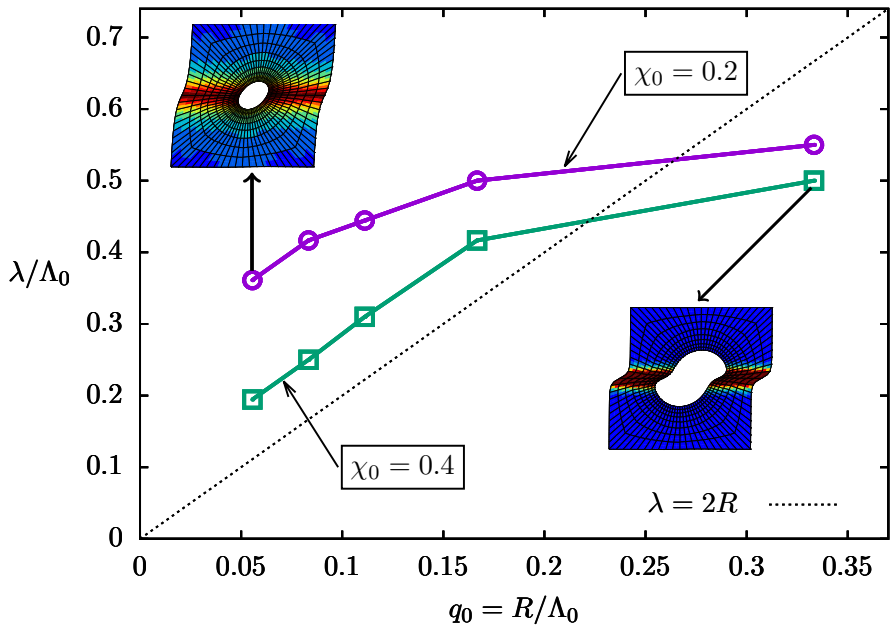

Fig. 12: Normalized localization slip band width λ as a function of q_0 for two different void volume fractions at the overall shear value $\overline{F}_{12} = 0.025$. Insets correspond to snapshots of figure 9i (left) and 9b (right) at $\overline{F}_{12} = 0.15$

In order to measure the influence of q_0 and χ_0 on the localization phenomenon, the localization slip band thickness is defined as

$$\lambda = \max_{x_1=0,x_2,x_3=0} \left(x_2^b - x_2^a, \Delta\gamma_{cum}(x_2^a) > \Delta\gamma_{cum}^{max}/15 \text{ and } \Delta\gamma_{cum}(x_2^b) > \Delta\gamma_{cum}^{max}/15\right) \quad (90)$$

$$\text{where} \quad \Delta\gamma_{cum}^{max} = \max_{x_1=0,x_2,x_3=0} (\Delta\gamma_{cum}(x_2)). \quad (91)$$

In other words, the band thickness is measured at 1/15 of the peak strain value. Figures 10 and 11 display the evolution of λ with the macroscopic strain for three values of q_0 at $\chi_0 = 0.2$ and $\chi_0 = 0.4$ respectively. For the two figures the dashed lines correspond to the limit where λ reaches four times the initial size along $\underline{\boldsymbol{X}}_2$ of the largest element inside the localization band. Therefore, results above this line can be considered as mesh independent, while it is considered mesh dependent when it goes below it. For both figures the top dashed line corresponds to $q_0 = 1/3$, the middle dashed line to $q_0 = 1/6$ and the bottom dashed line corresponds to $q_0 = 1/18$. Figure 12 shows the evolution of λ with q_0 at $\overline{F}_{12} = 2.5\%$ for two values of χ_0.

4.4. Discussion

4.4.1. Effect of intrinsic length and hole size on void shape

Figure 9 shows that void shape is significantly impacted both by q_0 and χ_0. For the lowest values of q_0, i.e. the lowest normalized void sizes, the holes remain elliptical, while they take peanut-like shapes when their size increases and become comparable with the intrinsic length scale. In addition increasing the porosity χ_0 induces preservation of elliptical void shapes for larger normalized void sizes. Eventually even for large void volume fractions peanut-like shapes are obtained. Peanut-like

void shapes are in good agreement with those observed inside dislocation channels (see figure 1a and 1b). However this agreement is for now only qualitative, and one must note that similar void shapes can be obtained with standard J2 flow theory.

4.4.2. Effect of intrinsic length and hole size on localized slip band width

Figure 10 and 11 show that, at a given porosity χ_0, larger values of normalized void size q_0 induce thicker localization slip bands. In addition increasing the porosity χ_0, for a given normalized void size q_0, decreases the localization slip band width.

Figure 12 shows more precisely that at a low macroscopic shear strain, larger normalized void sizes and/or smaller porosities induce thicker localization slip bands. The effect of the normalized void size can be understood as follows. When the void radius is much lower than Λ_0 the width of the localization zone is mainly governed by the void size. Hence, for small values of q_0, λ strongly depends on q_0. However when the void radius is of the order of magnitude of the intrinsic material length scale Λ_0 the width of the localization band is mainly governed by the latter parameter. Therefore a saturation of the localization band width is observed as q_0 increases. The effect of the porosity can be understood as follows. For a low porosity χ_0 the localization band width λ is expected to be close to the one of the sound material which has been shown in previous section to be equal to the intrinsic material length scale Λ_0. When increasing porosity χ_0, with void radii always smaller than the intrinsic material length scale ($q_0 = R/\Lambda_0 < 1$), voids are responsible of more intense flow localization and therefore localization bands are thinner than in the case of the sound material.

4.4.3. Effect of intrinsic length and hole size on the selection of slip and kink band modes

It can be seen in figure 9 that slip and kink bands, respectively parallel and perpendicular to the slip direction, initiate where the sheared material cross-section is reduced due to the presence of the void. In the simulations performed, kink bands were found to have a lower intensity than slip bands. It was proven by (Asaro and Rice, 1977) that slip and kink bands are equivalently probable at initiation of plastic slip for the problem considered. In the post-bifurcation simulations, the results clearly show that slip bands dominate at least for the considered configurations. This is probably due to the fact that, in contrast to slip band, kink bands are associated to strong lattice rotation and curvature so that their structure evolves rapidly with further overall straining Forest (1998); Forest et al. (2001). The present simulations show that the relative intensity of kink bands decreases when the macroscopic strain increases. As expected and according to (Ling et al., 2018) it is found that when decreasing the normalized void size q_0 the regularization power of the gradient model affects both kink and slip bands. For a given porosity χ_0 it is observed that the larger the normalized void size, the lower is the relative intensity of the kink band compared to the slip band. In addition it can be observed that, for a given normalized void size, the relative intensity of the kink band increases when increasing the porosity. It should be emphasized that the present model incorporates the effect of the spatial derivatives of the microslip both along and perpendicular to the slip plane. Gradient effects along the slip direction are related to the densities of geometrically necessary dislocations which are known to be responsible for

significant size effects. This contribution plays an essential role in the thickness of kink bands (Forest et al., 2001). In contrast gradient effects perpendicular to the slip planes are less explored even though they could be related to cross-slip (or climb at higher temperatures) of dislocations contributing to the finite thickness of slip band bundles (Neuhäuser, 1983a). The present model is isotropic with respect to the gradient of slip vector which essentially leads to the same finite thickness for slip and kink bands (see Ling et al. (2018)). A more elaborate formulation should introduce anisotropy and include a smaller length scale for slip bands than for kink bands.

5. Conclusions

The main findings of the present work can be summarized as follows:

1. The predictions of a micromorphic crystal plasticity model in case of single slip linear hardening for a periodic unit cell in simple shear have been established analytically. These analytical solutions have been used to validate the finite element implementation. Three cases were distinguished: linear hardening, perfect plasticity and linear softening. A fixed localization band width was shown to emerge in case of linear softening directly related to the higher order modulus of the micromorphic model.
2. A localization band widening has been observed in the finite element simulations at large strains when a non-linear saturating softening and a constant higher order modulus are considered. This band broadening has not been mentioned in the previous literature on plastic strain localization because most of the results in the literature are limited to linear softening and do not consider the saturating regime. It has been observed in the case of damage localization and cracking for some gradient damage model simulations. Such a broadening of plastic bands is not relevant for the simulation of continuing localization in slip bands observed for instance in irradiated materials.
3. An enhanced model is proposed in order to preserve a bounded localization band width when a non-linear saturating softening behaviour is used. It is based on a non-constant higher order modulus which varies with the cumulated plastic slip. Finite element results at large strains and an approximate analytical solution using such an evolving length scale confirm the absence of widening of the localization slip band in simple shear. The proposed constitutive function $A(\gamma_{cum})$ is decreasing toward zero which leads to a vanishingly small slip band width in the saturated regime. This is similar to existing gradient damage models based on an evolving and vanishing intrinsic length scale at fracture.
4. The enhanced model was applied to the study of void and slip band interaction. The effects of normalized void size and porosity versus intrinsic material length scale on the shape of deformed void, the localization band width, and the localized deformation pattern were illustrated by systematic micromorphic finite element simulations at large strains. Void shape was shown to evolve from elliptical towards peanut-like shape when increasing normalized void size or

decreasing void volume fraction which correspond to the experimental observation (see figure 1a). This model applied to a porous material has shown that the localization band width depends simultaneously on the intrinsic material length scale and the void size. Kink bands and slip bands are always observed at initiation of plastic slip and the relative intensity of slips bands compared to kink bands increases when increasing the macroscopic shear strain.

Future work will be dedicated to quantify the influence of several other physical parameters like the tensile versus shear stress ratio (i.e stress biaxiality), the slip system orientation and the number of active slip systems.

Arsenlis, A., Rhee, M., Hommes, G., Cook, R., Marian, J., 2012. A dislocation dynamics study of the transition from homogeneous to heterogeneous deformation in irradiated body-centered cubic iron. Acta Materialia 60, 3748–3757.

Asaro, R.J., Rice, J., 1977. Strain localization in ductile single crystals. Journal of the Mechanics and Physics of Solids 25, 309–338.

Audoly, B., Hutchinson, J.W., 2018. One-dimensional modeling of necking in rate-dependent materials. Journal of the Mechanics and Physics of Solids URL: http://www.sciencedirect.com/science/article/pii/S0022509618306586, doi:https://doi.org/10.1016/j.jmps.2018.08.005.

Bapna, M., Mori, T., Meshii, M., 1968. The observation of slip channels in quenched gold. Philosophical Magazine 17, 177–184.

Bardella, L., 2006. A deformation theory of strain gradient crystal plasticity that accounts for geometrically necessary dislocations. Journal of the Mechanics and Physics of Solids 54, 128–160.

Barton, N.R., Arsenlis, A., Marian, J., 2013. A polycrystal plasticity model of strain localization in irradiated iron. Journal of the Mechanics and Physics of Solids 61, 341–351.

Bažant, Z.P., Belytschko, T.B., Chang, T.P., 1984. Continuum theory for strain-softening. Journal of Engineering Mechanics 110, 1666–1692.

Besson, J., Foerch, R., 1997. Large scale object–oriented finite element code design. Computer Methods in Applied Mechanics and Engineering 142, 165–187.

Considère, A., 1885. Annales des Ponts et Chaussées 9 , 574–775.

Cordero, N., Gaubert, A., Forest, S., Busso, E.P., Gallerneau, F., Kruch, S., 2010. Size effects in generalised continuum crystal plasticity for two-phase laminates. Journal of the Mechanics and Physics of Solids 58, 1963–1994.

Cui, Y., Po, G., Ghoniem, N., 2018. Suppression of localized plastic flow in irradiated materials. Scripta Materialia 154, 34–39.

Dahlberg, C.F.O., Boasen, M., 2019. Evolution of the length scale in strain gradient plasticity. International Journal of Plasticity 112, 220 – 241. doi:doi.org/10.1016/j.ijplas.2018.08.016.

Erdle, H., Böhlke, T., 2017. A gradient crystal plasticity theory for large deformations with a discontinuous accumulated plastic slip. Computational Mechanics 60, 923–942.

Farrell, K., Byun, T., Hashimoto, N., 2003. Mapping flow localization processes in deformation of irradiated reactor structural alloys—final report. ORNL/TM-2003/63 .

Fish, R., Straalsund, J., Hunter, C., Holmes, J., 1973. Swelling and tensile property evaluations of high-fluence EBR-II thimbles, in: Effects of Radiation on Substructure and Mechanical Properties of Metals and Alloys. ASTM International. doi:doi.org/10.1520/STP35443S.

Fleck, N., Hutchinson, J., 1997. Strain gradient plasticity. Advances in Applied Mechanics 33, 296–361.

Forest, S., 1998. Modeling slip, kink and shear banding in classical and generalized single crystal plasticity. Acta Materialia 46, 3265–3281.

Forest, S., 2005. Generalized continua, in: Buschow, K.J., Cahn, R.W., Flemings, M.C., Ilschner, B., Kramer, E.J., Mahajan, S., Veyssière, P. (Eds.), Encyclopedia of Materials: Science and Technology. Elsevier, Oxford, pp. 1 – 7. URL: http://www.sciencedirect.com/science/article/pii/B008043152602091X, doi:https://doi.org/10.1016/B0-08-043152-6/02091-X.

Forest, S., 2008. Some links between Cosserat, strain gradient crystal plasticity and the statistical theory of dislocations. Philosophical Magazine 88, 3549–3563.

Forest, S., 2009. The micromorphic approach for gradient elasticity, viscoplasticity and damage. ASCE Journal of Engineering Mechanics 135, 117–131.

Forest, S., 2016. Nonlinear regularization operators as derived from the micromorphic approach to gradient elasticity, viscoplasticity and damage. Proc. R. Soc. A 472, 20150755.

Forest, S., Barbe, F., Cailletaud, G., 2000. Cosserat modelling of size effects in the mechanical behaviour of polycrystals and multiphase materials. International Journal of Solids and Structures 37, 7105–7126.

Forest, S., Boubidi, P., Sievert, R., 2001. Strain localization patterns at a crack tip in generalized single crystal plasticity. Scripta Materialia 44, 953–958.

Forest, S., Sedláček, R., 2003. Plastic slip distribution in two-phase laminate microstructures: dislocation-based versus generalized-continuum approaches. Philosophical Magazine 83, 245–276.

Geers, M., de Borst, R., Brekelmans, W., Peerlings, R., 1998. Strain-based transient-gradient damage model for failure analyses. Computer Methods in Applied Mechanics and Engineering 160, 133 – 153. URL: http://www.sciencedirect.com/science/article/pii/S004578259880011X, doi:https://doi.org/10.1016/S0045-7825(98)80011-X.

Germain, N., Besson, J., Feyel, F., 2007. Simulation of laminate composites degradation using mesoscopic non-local damage model and non-local layered shell element. Modelling and Simulation in Materials Science and Engineering 15, S425.

Germain, P., 1973. The method of virtual power in continuum mechanics. Part 2: Microstructure. SIAM Journal on Applied Mathematics 25, 556–575.

Gilman, J., 1954. Mechanism of ortho kink-band formation in compressed zinc monocrystals. JOM 6, 621–629.

Gurtin, M.E., 2000. On the plasticity of single crystals: free energy, microforces, plastic-strain gradients. Journal of the Mechanics and Physics of Solids 48, 989–1036.

Gurtin, M.E., 2002. A gradient theory of single-crystal viscoplasticity that accounts for geometrically necessary dislocations. Journal of the Mechanics and Physics of Solids 50, 5–32.

Gussev, M.N., Field, K.G., Busby, J.T., 2015. Deformation localization and dislocation channel dynamics in neutron-irradiated austenitic stainless steels. Journal of Nuclear Materials 460, 139–152.

Hadamard, J., 1903. Leçons sur la propagation des ondes et les équations de l'hydrodynamique. Paris, Librairie Scientifique A. Hermann .

Hart, E., 1967. Theory of the tensile test. Acta Metallurgica 15, 351 – 355. URL: http://www.sciencedirect.com/science/article/pii/0001616067902118, doi:https://doi.org/10.1016/0001-6160(67)90211-8.

Hill, R., 1962. Acceleration waves in solids. Journal of the Mechanics and Physics of Solids 10, 1–16.

Jaoul, B., (1965, 2008). Etude de la plasticité et application aux métaux. Presses des MINES.

Jiao, Z., Was, G., 2010. The role of irradiated microstructure in the localized deformation of austenitic stainless steels. Journal of Nuclear Materials 407, 34–43.

Lee, E., Byun, T., Hunn, J., Yoo, M., Farrell, K., Mansur, L., 2001. On the origin of deformation microstructures in austenitic stainless steel: Part I–microstructures. Acta Materialia 49, 3269 – 3276. URL: http://www.sciencedirect.com/science/article/pii/S1359645401001938, doi:https://doi.org/10.1016/S1359-6454(01)00193-8.

Ling, C., Forest, S., Besson, J., Tanguy, B., Latourte, F., 2018. A reduced micromorphic single crystal plasticity model at finite deformations. application to strain localization and void growth in ductile metals. International Journal of Solids and Structures 134, 43–69.

Ling, C., Tanguy, B., Besson, J., Forest, S., Latourte, F., 2017. Void growth and coalescence in triaxial stress fields in irradiated fcc single crystals. Journal of Nuclear Materials 492, 157–170.

Lorentz, E., Benallal, A., 2005. Gradient constitutive relations: numerical aspects and application to gradient damage. Computer Methods in Applied Mechanics and Engineering 194, 5191 – 5220. URL: http://www.sciencedirect.com/science/article/pii/S0045782505000307, doi:https://doi.org/10.1016/j.cma.2004.12.016.

Luft, A., Richter, J., Schlaubitz, K., Loose, C., Mühlhaus, C., 1975. Work softening and microstructural instability of predeformed molybdenum single crystals. Materials Science and Engineering 20, 113–122.

Mandel, J., 1966. Conditions de stabilité et postulat de Drucker, in: Rheology and Soil Mechanics/Rhéologie et Mécanique des Sols. Springer, pp. 58–68.

McMurtrey, M., Was, G., Patrick, L., Farkas, D., 2011. Relationship between localized strain and irradiation assisted stress corrosion cracking in an austenitic alloy. Materials Science and Engineering: A 528, 3730 – 3740. URL: http://www.sciencedirect.com/science/article/pii/S0921509311000955, doi:https://doi.org/10.1016/j.msea.2011.01.073.

Mori, T., Meshii, M., 1969. Plastic deformation of quench-hardened aluminum single crystals. Acta Metallurgica 17, 167–175.

Neuhäuser, H., 1983a. Dislocations in Solids, Vol. 6, F.R.N. Nabarro, Editor. North-Holland Publishing Company, Amsterdam. chapter The dynamics of slip band formation in single crystals. pp. 319–440.

Neuhäuser, H., 1983b. Slip-line formation and collective dislocation motion, in dislocations in solids, vol 4 edited by F. R. N. Nabarro.

Niordson, C.F., Kysar, J.W., 2014. Computational strain gradient crystal plasticity. Journal of the Mechanics and Physics of Solids 62, 31–47.

Petryk, H., Stupkiewicz, S., 2016. A minimal gradient-enhancement of the classical continuum theory of crystal plasticity. Part I: The hardening law. Archives of Mechanics 68, 459–485.

Poh, L.H., Sun, G., 2017. Localizing gradient damage model with decreasing interactions. International Journal for Numerical Methods in Engineering 110, 503–522.

Renault-Laborne, A., Hure, J., Malaplate, J., Gavoille, P., Sefta, F., Tanguy, B., 2018. Tensile properties and deformation microstructure of highly neutron-irradiated 316 stainless steels at low and fast strain rate. Journal of Nuclear Materials 508, 488 – 504. URL: http://www.sciencedirect.com/science/article/pii/S0022311518301430, doi:https://doi.org/10.1016/j.jnucmat.2018.05.068.

Rice, J.R., 1976. The localization of plastic deformation, in: Koiter, W.T. (Ed.), Theoretical and Applied Mechanics (Proceedings of the 14th International Congress on Theoretical and Applied Mechanics), North-Holland Publishing CO.. pp. 207–220.

Simone, A., Askes, H., Sluys, L.J., 2004. Incorrect initiation and propagation of failure in non-local and gradient-enhanced media. International Journal of Solids and Structures 41, 351 – 363. URL: http://www.sciencedirect.com/science/article/pii/S0020768303005213, doi:https://doi.org/10.1016/j.ijsolstr.2003.09.020.

Smidt Jr, F., 1970. Comments on dislocation structures in irradiated and strained iron. Scripta Metallurgica 4, 517–520.

Steinmann, P., Stein, E., 1996. On the numerical treatment and analysis of finite deformation ductile single crystal plasticity. Computer Methods in Applied Mechanics and Engineering 129, 235–254.

Stelmashenko, N., Walls, M., Brown, L., Milman, Y.V., 1993. Microindentations on W and Mo oriented single crystals: A STM study. Acta Metallurgica et Materialia 41, 2855–2865.

Thomas, T.Y., 1961. Plastic Flow and Fracture in Solids. volume 2. Elsevier.

Tucker, R., Wechsler, M., Ohr, S., 1969. Dislocation channeling in neutron-irradiated niobium. Journal of Applied Physics 40, 400–408.

Vandoren, B., Simone, A., 2018. Modeling and simulation of quasi-brittle failure with continuous anisotropic stress-based gradient-enhanced damage models. Computer Methods in Applied Mechanics and Engineering 332, 644–685.

Wechsler, M.S., 1973. Dislocation channeling in irradiated and quenched metals. The Inhomogeneity of Plastic Deformation .

Wulfinghoff, S., Bayerschen, E., Böhlke, T., 2013. A gradient plasticity grain boundary yield theory. International Journal of Plasticity 51, 33–46.

Wulfinghoff, S., Böhlke, T., 2012. Equivalent plastic strain gradient enhancement of single crystal plasticity: theory and numerics. Proc. R. Soc. A 468, 2682–2703.

Wulfinghoff, S., Forest, S., Böhlke, T., 2015. Strain gradient plasticity modeling of the cyclic behavior of laminate microstructures. Journal of the Mechanics and Physics of Solids 79, 1–20.

Z–set package, 2013. Non-linear material & structure analysis suite, www.zset-software.com .

Zbib, H.M., Aifantis, E.C., 1988. On the structure and width of shear bands. Scripta Metallurgica 22, 703–708.